The Cold Ocean–Warm Land Pattern: Model Simulation and Relevance to Climate Change Detection

ANTHONY J. BROCCOLI, NGAR-CHEUNG LAU, AND MARY JO NATH

Geophysical Fluid Dynamics Laboratory/NOAA, Princeton University, Princeton, New Jersey

(Manuscript received 2 July 1997, in final form 8 January 1998)

ABSTRACT

Surface air temperatures from a 1000-yr integration of a coupled atmosphere–ocean model with constant forcing are analyzed by using a method that decomposes temperature variations into a component associated with a characteristic spatial structure and a residual. The structure function obtained from the coupled model output is almost identical to the so-called cold ocean–warm land (COWL) pattern based on observations, in which above-average spatial mean temperature is associated with anomalously cold oceans and anomalously warm land. This pattern features maxima over the high-latitude interiors of Eurasia and North America. The temperature fluctuations at the two continental centers exhibit almost no temporal correlation with each other. The temperature variations at the individual centers are related to teleconnection patterns in sea level pressure and 500-mb height that are similar to those identified in previous observational and modeling studies. As in observations, variations in the polarity and amplitude of this structure function are an important source of spatially averaged surface air temperature variability.

Results from parallel integrations of models with more simplified treatments of the ocean confirm that the contrast in thermal inertia between land and ocean is the primary factor for the existence of the COWL pattern, whereas dynamical air–sea interactions do not play a significant role. The internally generated variability in structure function amplitude in the coupled model integration is used to assess the importance of the upward trend in the amplitude of the observed structure function over the last 25 yr. This trend, which has contributed to the accelerated warming of Northern Hemisphere temperature over recent decades, is unusually large compared with the trends generated internally by the coupled model. If the coupled model adequately estimates the internal variability of the real climate system, this would imply that the recent upturn in the observed structure function may not be purely a manifestation of unforced variability. A similar monotonic trend occurs when the same methodology is applied to a model integration with time-varying radiative forcing based on past and future CO_2 and sulfate aerosol increases. This finding illustrates that this decomposition methodology yields ambiguous results when two distinct spatial patterns, the ''natural'' COWL pattern (i.e., that associated with internally generated variability) and the anthropogenic fingerprint, are present in the simulated climate record.

1. Introduction

The instrumental climate record contains evidence of variations on a wide range of spatial and temporal scales. Of much interest is the persistent warming trend that extends through much of the past 100 years. This trend has been linked to the radiative forcing associated with the ongoing increases in the concentrations of a variety of greenhouse gases, most notably CO_2 (Santer et al. 1996). However, there are many other potential sources of climate variability. Forced variations can result from solar variability, volcanic aerosols, and vegetation changes. In addition, the internal dynamics of the climate system is capable of producing unforced fluctuations. The El Niño–Southern Oscillation (ENSO) phenomenon, which is associated with large-amplitude atmospheric and oceanic changes affecting vast expanses of the earth's surface (Rasmusson and Carpenter 1982; Philander 1990), is a noteworthy example of internal variability. Other interactions among different components of the atmosphere–ocean–land system may also contribute to the rich spectrum of climate variability (e.g., Mann and Park 1994, 1996; Mann et al. 1995; Parker et al. 1994; Trenberth and Hurrell 1994; Schlesinger and Ramankutty 1994). To clearly identify the origin of the global warming trend, it is important to discern as many other sources of climate variability as possible and recognize their individual signatures in the climate record, so that any radiatively induced changes can be isolated.

Recently, Wallace et al. (1995, hereafter WZR) analyzed observed temperature data in an attempt to better isolate long-term variations in Northern Hemisphere mean temperature. They found that much of the month-to-month variability that dominates the temperature time series is associated with a spatial pattern in which the

Corresponding author address: Dr. Anthony J. Broccoli, GFDL/NOAA, Princeton University, P.O. Box 308, Forrestal Campus, U.S. Rt. 1, Princeton, NJ 08542.
E-mail: ajb@gfdl.gov

extratropical temperature anomalies over land and ocean are of opposite sign. Specifically, when the hemisphere is warm, the oceans are anomalously cold and the continents are anomalously warm. This pattern, dubbed the cold ocean–warm land (COWL) pattern, is responsible for approximately half of the temporal variance in monthly mean hemispherically averaged surface air temperature. WZR speculated that the variability associated with the COWL pattern results from atmospheric dynamics and the contrast in thermal inertia between continents and oceans. They argued that lower frequency fluctuations in global mean temperature, such as long-term trends and interdecadal variability, could be isolated by removing the variations associated with the COWL pattern. Furthermore, WZR argued that the strong COWL-related contribution to the observed upward trend in hemispheric mean temperature during the 1970s and 1980s was not necessarily linked to radiatively induced global warming.

If the interpretations of WZR are correct, the removal of the COWL pattern signature from the global temperature record would constitute an effective method to detect anthropogenic climate change. Thus it is desirable to further test some of the interpretations of WZR. Climate models offer a means for such testing. Models allow hypotheses to be critically examined in more controlled settings than can be provided by observational data alone. Furthermore, the model simulations are not subject to the limitations associated with incomplete observational networks. For this approach to be successful, however, it is important that the climate model be capable of capturing the essence of the observed climate variability. For comparison with the results of WZR, the ability to produce a credible simulation of variability on timescales from intraseasonal through decadal is a necessary condition.

At the Geophysical Fluid Dynamics Laboratory, a very long integration (~1000 yr) of a coupled atmosphere–ocean model has been made for the purpose of exploring climate variability (Stouffer et al. 1994; Manabe and Stouffer 1996). The power spectrum of global mean surface air temperature from this integration has been compared to its observed counterpart and found to be reasonably realistic (Manabe and Stouffer 1996), although the amplitude of ENSO-related variability is underestimated (Knutson et al. 1997). Other studies have demonstrated that the atmospheric component of this model is capable of simulating atmospheric variability on daily to seasonal timescales (Manabe and Hahn 1981; Lau 1981; Lau and Nath 1987) and reproducing realistic circulation patterns in response to tropical sea surface temperature (SST) variations (Lau 1985; Lau and Nath 1994).

Thus we believe that it is appropriate to apply the analysis techniques introduced by WZR to the output from the 1000-yr integration of the coupled atmosphere–ocean model mentioned above. Our purpose is to determine the role of the COWL pattern as a source of month-to-month surface air temperature variability in the model, and to explore the physical mechanisms responsible for its existence. We will examine the importance of air–sea interaction by applying the same analysis techniques to other integrations in which simpler representations of the ocean have been substituted for the complete ocean general circulation model. In addition, we will use a coupled model integration forced by estimated variations in greenhouse gas and tropospheric sulfate aerosol forcing (Haywood et al. 1997) to test WZR's hypothesis that removal of the contribution from the COWL pattern allows radiatively forced temperature trends to be isolated more clearly.

The remainder of the paper is organized as follows. Section 2 and the appendix contain a mathematical description of the method introduced by WZR and its relationship to standard statistical techniques. In section 3 this method is applied to both the coupled model integration and observed data, and a comparison is made between the two sets of results. The physical processes responsible for the existence of the COWL pattern, as well as the relationship of this pattern to other manifestations of atmospheric variability, are explored in section 4. Section 5 examines the recent observed warming trend in the context of the simulated variability associated with the COWL pattern. Section 6 contains an assessment of the impact of anthropogenic radiative forcing from greenhouse gases and sulfate aerosols on the signature of the COWL pattern. The paper concludes with a summary and discussion in section 7.

2. Methodology

Our primary purpose is to search for a single spatial pattern with temporal variability that is closely related to fluctuations of the spatially averaged surface temperature field. The identification of this pattern facilitates the partitioning of the time series of the spatially averaged temperature into two components. The first component represents the contribution of the temporal changes in the amplitude and polarity of the characteristic structure function. The second component is the residual arising from this fitting procedure. In the present article, this decomposition is performed by following the same methodology developed in WZR. The notation used here is also identical to that adopted in WZR, with $\overline{(\,)}$ and $\langle\,\rangle$ indicating spatial and temporal averaging, respectively, x representing the two-dimensional (latitude–longitude) space variable, and t the time variable. In computing the spatial averages, the value at each grid point is weighted by the cosine of latitude for that point.

To accomplish the goal stated above, we first express the space–time variations of the surface temperature anomaly field $T(x, t)$ as the sum of two terms: the product between a spatial function $A(x)$ and a time series of expansion coefficients $T_1(t)$, and the residual field, $\delta(x, t)$; that is,

$$T(x, t) = A(x)T_1(t) + \delta(x, t). \quad (1)$$

Here, $A(x)$ can be written as the sum of its spatial average and deviations from this spatial average; that is, $A(x) = \overline{A} + A^*(x)$, with $\overline{A^*(x)} = 0$. Performing a spatial average of Eq. (1), then yields

$$\overline{T}(t) = \overline{A}T_1(t) + T_0(t), \quad (2)$$

where $T_0(t) = \overline{\delta(x, t)}$. By subtracting Eq. (2) from Eq. (1), we obtain

$$T^*(x, t) = A^*(x)T_1(t) + \delta^*(x, t), \quad (3)$$

where $\delta^*(x, t) = \delta(x, t) - \overline{\delta(x, t)}$.

It is important to note that the same time series of expansion coefficients $T_1(t)$ appear in the first term on the rhs of Eqs. (1), (2), and (3). Although Eq. (2) exhibits no explicit spatial dependence, the presence of this common time series in the term $\overline{A}T_1(t)$ in this equation signifies that fluctuations of the spatial pattern $A(x)$ do contribute to the variability of $\overline{T}(t)$. Hence Eq. (2) is in effect the desired decomposition mentioned in the beginning of this section; it expresses $\overline{T}(t)$ as the sum of a component associated with temporal changes in a structure function [i.e., $\overline{A}T_1(t)$] and a residual [$T_0(t)$].

To compute various quantities of interest (see details in the appendix), certain assumptions need to be made on the relationship between the residual and the component associated with temporal changes in $A(x)$. First, we require that the two terms resulting from the decomposition of $\overline{T}(t)$ in Eq. (2) be orthogonal to each other in the temporal domain. As a result of this requirement, the spatial mean of the residual [$\overline{\delta(x, t)}$, or $T_0(t)$] exhibits no temporal correlation with $\overline{A}T_1(t)$, or

$$\langle T_0(t)T_1(t)\rangle = 0. \quad (4)$$

Second, we require that the two components of $T^*(x, t)$ on the rhs of Eq. (3) be mutually orthogonal in the spatial domain, so that deviation of the residual at all t from its spatial mean [$\delta^*(x, t)$] has no spatial projection on $A^*(x)$, or

$$\overline{\delta^*(x, t)A^*(x)} = 0. \quad (5)$$

In the following sections, we shall present the spatial pattern $A(x)$ as well as the time series $T_1(t)$ and $T_0(t)$ using observations and model output for selected data domains. The computational details for obtaining these quantities are given in the appendix. It is also demonstrated in the appendix that the procedure described therein is equivalent to a singular value composition analysis, with the left and right input fields corresponding to $\overline{T}(t)$ and $T^*(x, t)$, respectively.

Although we have adopted the methodology of WZR in the present study, it is worth noting that the covariability between local temperature fluctuations and $\overline{T}(t)$ could also be analyzed using other conventional techniques. One example of the more standard approaches is to compute the spatial pattern of the regression coefficients of $T(x, t)$ at individual grid points on the area-averaged index $\overline{T}(t)$, as was done by Manabe and Stouffer (1996). It can be shown that the regression pattern thus obtained is linearly related to the structure function $A(x)$ examined here.

3. Simulation of the COWL pattern

The simulated data to be examined here are primarily generated by the coupled atmosphere–ocean model developed at the Geophysical Fluid Dynamics Laboratory. This model has been used in a variety of studies of climate change and climate variability (Stouffer et al. 1989; Manabe et al. 1991, 1992; Manabe and Stouffer 1993, 1994, 1996; Delworth et al. 1993; Knutson and Manabe 1994, 1995; Knutson et al. 1997). For brevity, it will be called the coupled model in subsequent references. The model consists of an atmospheric general circulation model based on the spectral transform method coupled with a finite-difference general circulation model of the ocean. Heat, water, and snow budgets for continental surfaces are computed, and the seasonal (but not diurnal) cycle of solar radiation is prescribed at the top of the model atmosphere. The horizontal resolution of the atmospheric component is determined by the truncation limit; in this case the so-called rhomboidal truncation at wavenumber 15 (R15) is used. Vertical variations in the model atmosphere are represented at nine sigma levels. In the oceanic component, the finite-difference grid has a spacing of approximately 4.5° lat × 3.7° long, and there are 12 unevenly spaced levels in the vertical. The model has realistic geography, surface topography, and bathymetry, consistent with its computational resolution. To reduce climate drift, the fluxes of heat and water across the air–sea interface are modified by amounts that vary spatially and seasonally, but do not vary from one year to the next. These flux adjustments are determined prior to integrating the coupled model, and are not correlated with the transient anomalies of temperature or salinity that evolve during the coupled model integration. Details of the model structure, method of time integration, and performance are described by Manabe et al. (1991).

For comparison with the results of WZR, the method outlined in section 2 and the appendix is applied to the output from a 1000-yr integration of the model described above in which external forcing is held constant (Manabe and Stouffer 1996). Thus, only unforced climate variations resulting from the internal dynamics of the coupled model are present, except for a very slow drift that probably results from imperfect initialization techniques. One of the manifestations of this drift is a trend of -2.3×10^{-4} °C yr^{-1} in global mean surface air temperature; for reference, this is approximately 20 times smaller than the observed temperature trend during the twentieth century.

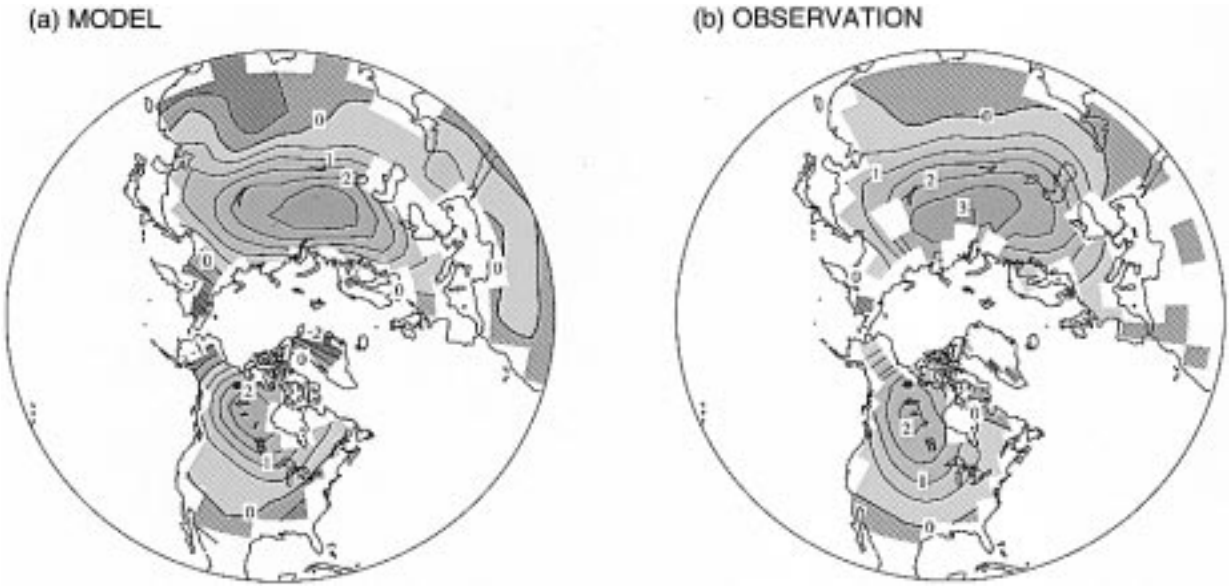

FIG. 1. Distribution of the structure function $A(x)$ for surface air temperature from (a) the 1000-yr coupled model integration, and (b) observations during the 1900–95 period. In both cases, the spatial domain of the analysis is restricted to land north of 20°N. Contour interval is 0.5. Positive (negative) values are shaded in red (blue). Unshaded land areas in (b) correspond to sites with inadequate data records during 1900–95.

a. Northern Hemisphere land (20°–90°N)

Mean monthly surface air temperatures for each of the 12 000 months of the coupled model integration serve as input to the analysis. The global temperature dataset of Jones and Briffa (1992), as extended through 1995, is also analyzed to facilitate comparisons between the model and observations. This dataset utilizes SST data in addition to surface air temperature data from land stations to extend its spatial coverage to oceanic regions. For consistency with WZR, the spatial domain of the analysis is limited to Northern Hemisphere land points north of 20°N.

The structure function $A(x)$ is computed based on output from the coupled model integration (Fig. 1a) and the observed temperature data for the period 1900–95 (Fig. 1b). (Note that the pattern in Fig. 1b is very similar to that in Fig. 3 of WZR, which depicts the related quantity $A(x)/\overline{A}$ based on the same observations from a slightly shorter period.) A high degree of similarity exists between the simulated and observed $A(x)$ patterns, with prominent positive centers over the northern interiors of Eurasia and North America, and weaker negative values in most locations south of 30°N and over some coastal regions at higher latitudes. The quantitative values of $A(x)$ in the Eurasian and North American maxima are also very similar in the simulated and observed results. When the analysis domain is expanded by including both land and ocean sites, WZR (see their Fig. 4) reported that the observed pattern of $A(x)$ is closely related to the underlying land–sea contrast. In particular, positive values of $A(x)$ prevail over the continental interiors, whereas negative values are mostly found in maritime regions. This characteristic distribution has led WZR to coin the term ''cold ocean–warm land pattern.''

To enable the reader to maintain the connection between this paper and the previous work by WZR, the following terminology is defined. ''COWL pattern'' refers to the structure function $A(x)$ computed from observations, as this is the terminology introduced by WZR. The $A(x)$ computed from the coupled model integration will also be called the COWL pattern because of its similarity to the observed $A(x)$. In keeping with this terminology, the time series $\overline{A}T_1(t)$ (computed from either observations or the coupled model) may also be regarded as the contribution of variations in the amplitude and polarity of the COWL pattern to spatially averaged temperature fluctuations. This terminology will be used consistently in the remainder of the paper, and should not be construed to imply any particular physical origin for this pattern.

Time series of the quantities $\overline{T}(t)$, $\overline{A}T_1(t)$, and $T_0(t)$ provide information on the contribution of the COWL pattern to the variability of hemispheric mean land temperature. They are displayed in Fig. 2 for a representative 200-yr segment of the coupled model integration and for observations from the period 1900–95. The value for each month is indicated by a single dot, with the blue and red dots corresponding to months in the cold season (November–April) and warm season (May–October), respectively. Autocorrelation functions for each of these three time series are also computed from the coupled model (Fig. 3a) and observations (Fig. 3b). (For reference, Figs. 2b and 3b of this paper correspond to Figs. 1 and 2 of WZR, respectively.)

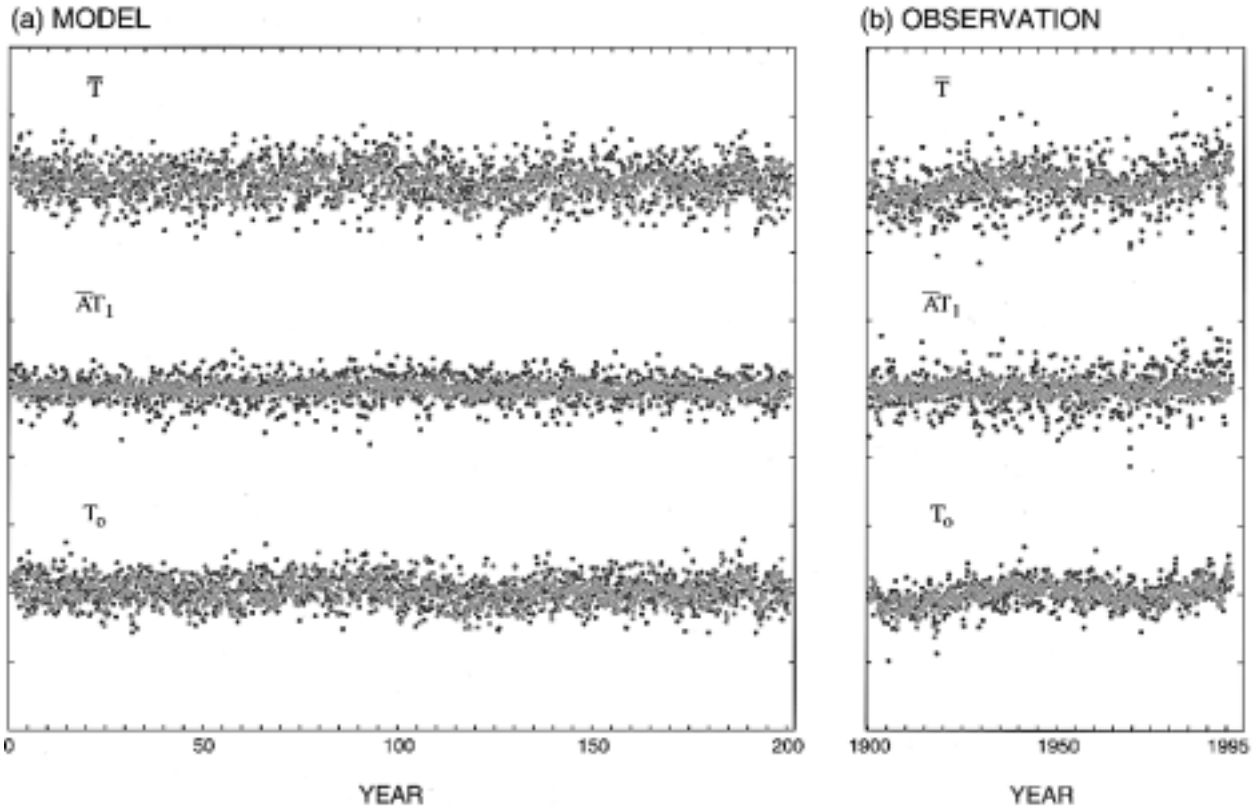

FIG. 2. Time series of $\overline{T}(t)$, $\overline{A}T_1(t)$, and $T_0(t)$ from (a) a representative 200-yr segment of the coupled model integration and (b) observations. Monthly data for cold season months (November–April) are indicated by blue dots, and data for warm season months (May–October) are indicated by red dots overprinted on the blue. The interval between tick marks on the ordinate is 1°C.

In both the coupled model and observations, the hemispheric mean temperature $\overline{T}(t)$ exhibits considerable month-to-month scatter, particularly in the cold season. This scatter is comparable in magnitude to the observed warming trend during the twentieth century, and thus adds to the difficulty of trend detection. The autocorrelation functions based on simulated and observed $\overline{T}(t)$ indicate the presence of low-frequency variability, as evident from the positive autocorrelations at lag intervals through 60 months. The autocorrelations remain much higher at longer lags for the observed $\overline{T}(t)$, primarily because the century-scale warming trend in that time series is much larger than the very slow drift in the coupled model temperatures. Autocorrelations from a linearly detrended version of the observed $\overline{T}(t)$ time series (not shown) closely resemble those from the coupled model.

The characteristics of $\overline{A}T_1(t)$ are quite different from those of $\overline{T}(t)$, as can be seen by both visual inspection of the plotted time series and the autocorrelation functions. For both the simulated and observed data, the autocorrelation function of $\overline{A}T_1(t)$ diminishes rapidly with increasing lag and becomes quite small after just a few months. The long-term trend evident in the observed $\overline{T}(t)$ is virtually absent in $\overline{A}T_1(t)$ before 1970 (see Fig. 2b), although there is evidence of an upward trend in $\overline{A}T_1(t)$ during the cold season in recent decades.

The standard deviation of $\overline{A}T_1(t)$ during the cold season is ~2.5 times larger than the warm season in both the coupled model and observations, indicating that the COWL pattern is a much more important source of hemispheric mean temperature variability during the winter months. When all months are considered, $\overline{A}T_1(t)$ accounts for 58% of the variance of the observed $\overline{T}(t)$.[1] For the coupled model, the explained variance is somewhat smaller at 37% (Table 1).

Most of the low-frequency variability in hemispheric mean temperature is found in the residual term $T_0(t)$ that is obtained by subtracting the contribution of the COWL pattern $\overline{A}T_1(t)$ from $\overline{T}(t)$ [see Eq. (2)]. This is evident visually in the time series plot of the observed $T_0(t)$ (Fig. 2b), in which the familiar pattern of warming from the beginning of the century through the 1940s, cooling from the mid-1940s through the mid-1970s, and

[1] Note that this fraction is larger than the 46% reported by WZR. A close comparison reveals that this difference arises from our use of a dataset with higher spatial resolution and the extension of the analysis through 1995.

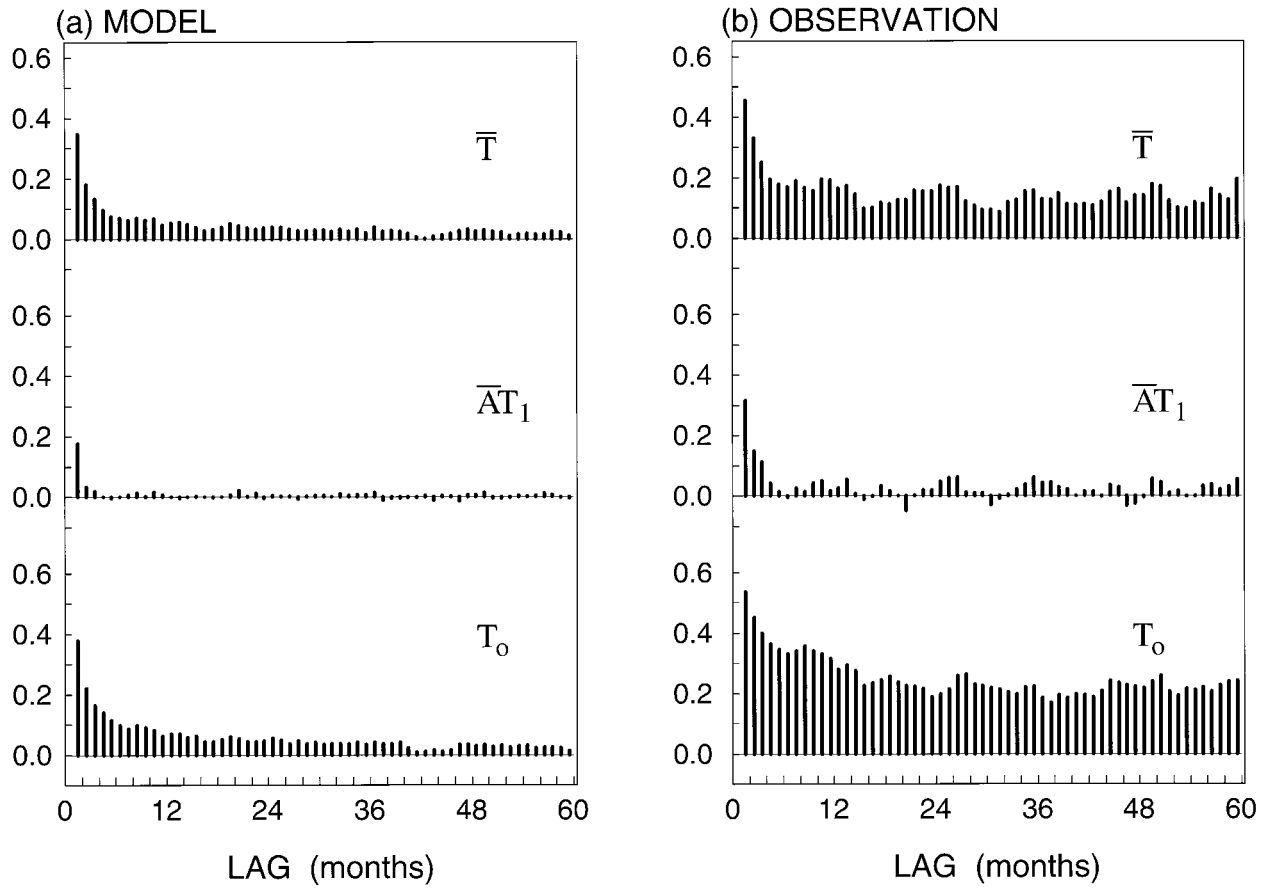

FIG. 3. Autocorrelation functions for the time series plotted in Fig. 2. Lags are given in months.

a warming trend thereafter is readily apparent. The autocorrelation functions from both the coupled model and observations also indicate the prevalence of low-frequency variability in $T_0(t)$, as the autocorrelation values for longer lags are much higher than those computed from $\overline{A}T_1(t)$, particularly for observations. Autocorrelation values for $T_0(t)$ are also slightly larger than those for $\overline{T}(t)$ in both coupled models and observations. In general, the coupled model is able to reproduce the gross characteristics of $\overline{T}(t)$, $\overline{A}T_1(t)$, and $T_0(t)$, providing further evidence from a model perspective that, in the absence of any trends in external forcing, the removal of the COWL pattern may be an effective means of highlighting low-frequency variability.

TABLE 1. Ratio (in percent) of variance in $\overline{A}T_1(t)$ vs variance in $\overline{T}(t)$, as computed for various analysis domains and model or observational datasets. The computations are based on all months of the year.

Data	20°–90°N land only	20°–90°N land and ocean	Global land and ocean
Observed	58	48	36
Coupled integration	37	43	30
Mixed layer (ML) integration	—	39	—
Fixed SST (FS) integration	—	47	—

b. Other spatial domains

The preceding analysis can be extended to other spatial domains to determine if the structure of the COWL pattern is domain dependent. As a first step, the southern boundary of the analysis domain is kept at 20°N but temperatures from ocean grid points are included along with those from land. The resulting structure function $A(x)$ (Fig. 4a) bears a very strong resemblance to that computed from land points only (Fig. 1a). Prominent maxima are located over the high-latitude interiors of Eurasia and North America, with a minimum centered north of Iceland and extending over the nearby portions of the Norwegian Sea and adjacent waters. Slightly weaker minima are found over the central North Pacific and the Gulf of Mexico. Positive values of $A(x)$ are almost completely restricted to the middle- to high-latitude continents, with the only exception being an area of positive values extending from Alaska and the Canadian archipelago across the Arctic to Siberia. The positive values over this portion of the Arctic may be

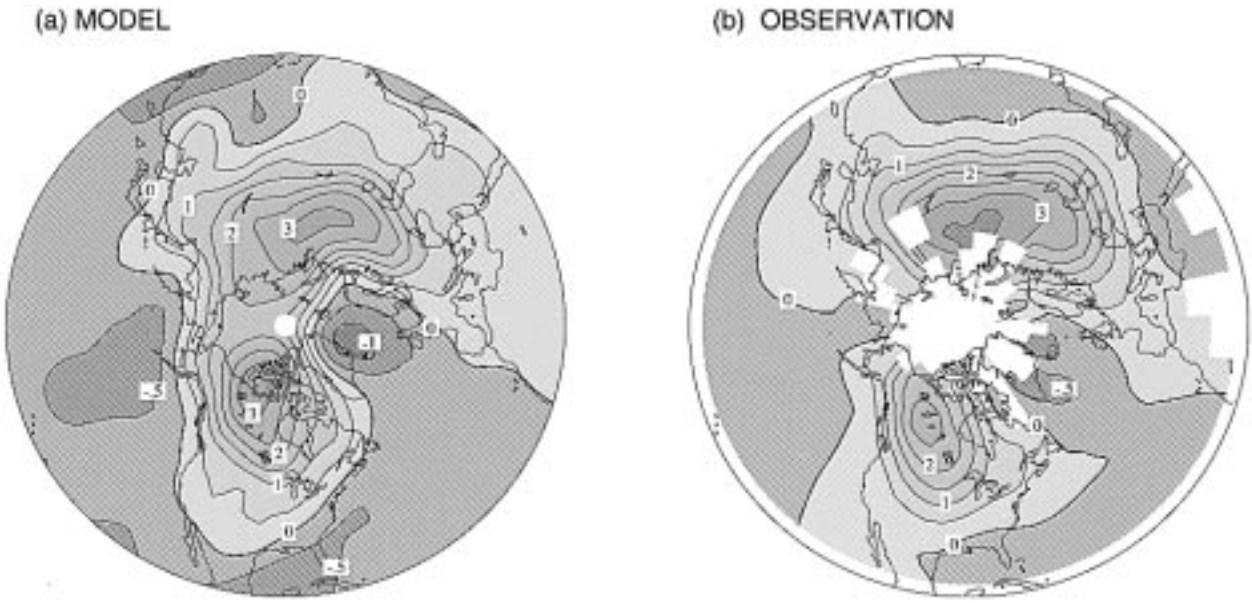

FIG. 4. Same as Fig. 1 except that analysis domain includes all grid points north of 20°N.

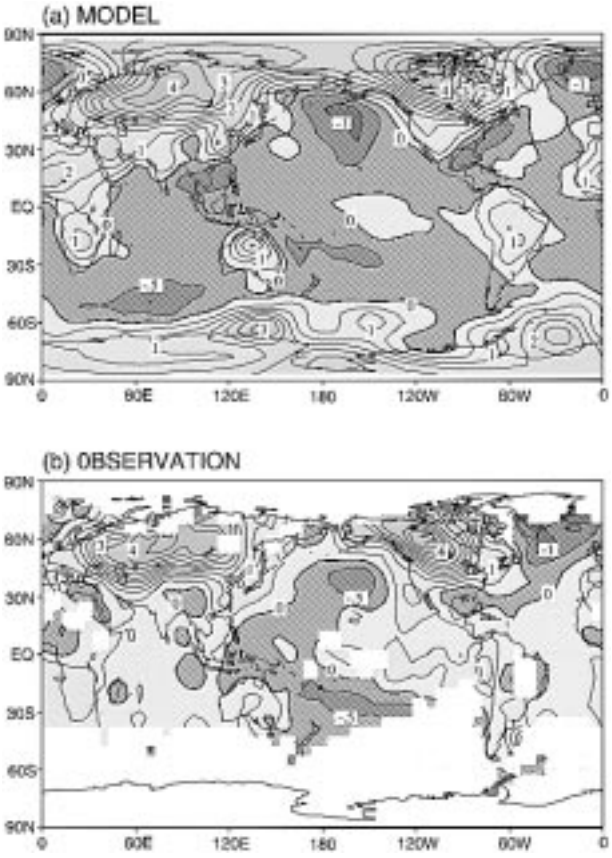

FIG. 5. Same as Fig. 1 except that analysis domain is global and unshaded areas in (b) correspond to sites with inadequate data records during 1900–95.

related to the presence of sea ice in this region, which possesses surface characteristics similar to a continental surface during the cold season. Negative values dominate over all other ocean grid points in the domain, as well as many coastal areas and portions of the subtropical continents. Most of these characteristics also appear in the $A(x)$ pattern computed from observations using the same domain (Fig. 4b).

When the analysis domain is extended further to encompass the entire globe, the spatial pattern of $A(x)$ simulated by the coupled model in the Northern Hemisphere extratropics is similar to that computed using the more restricted domains (Fig. 5a). Prominent positive centers occupy the high-latitude interiors of Eurasia and North America, with mainly negative values over the North Pacific and North Atlantic Oceans. Elsewhere, the $A(x)$ pattern simulated by the coupled model features positive values over the continents, with local maxima over northern Africa, Australia, and northern South America. A complex pattern of positive values also covers Antarctica and nearby portions of the Southern Ocean, primarily over ice-covered regions. Negative values of $A(x)$ dominate over most oceanic regions, with the only sizeable exception being an area of weak positive values over the eastern and central tropical Pacific. Negative values are also noted in those continental regions where maritime influences are strong, such as southeastern Asia, Central America, and southern South America.

The observed $A(x)$ pattern based on a global analysis domain (Fig. 5b) has both similarities and differences with respect to the pattern simulated by the coupled model. As in the model, the observed $A(x)$ pattern in the Northern Hemisphere extratropics is dominated by

the positive centers over the continental interiors, with a tendency for negative values over the adjacent oceans, particularly over the central North Pacific and high-latitude North Atlantic. In general, the prevalence of negative values over most ice-free oceanic regions in the simulated $A(x)$ pattern does not appear in the observed $A(x)$ pattern. The two patterns do share the tendency for positive $A(x)$ values over the central and eastern tropical Pacific, with negative values surrounding this area to the north, west, and south. This pattern, which is reminiscent of the signature of ENSO variability or Pacific interdecadal variability (Zhang et al. 1997; Knutson et al. 1997), is less pronounced in the coupled model simulation. Over the Southern Hemisphere continents, the pattern is rather patchy, although there may be a tendency for $A(x)$ values to be predominately positive. Some caution is required in comparing the simulated and observed patterns because of the paucity of observations in the Southern Hemisphere extratropics and the use of SST as a substitute for surface air temperatures in the observational data.

Comparison of the $A(x)$ patterns based on different spatial domains indicates that the COWL pattern remains dominant as the analysis domain is expanded beyond the extratropical Northern Hemisphere. The domain-independence of this pattern supports the assertion that the COWL pattern is not simply an artifact of averaging only over Northern Hemisphere land when determining the spatial mean temperature. Both in the coupled model and in observations, spatial mean temperature fluctuations associated with the COWL pattern [i.e., $\overline{A}T_1(t)$] make substantial contributions to the total variance of spatial mean temperature irrespective of analysis domain (Table 1). Thus the COWL pattern appears to be a robust feature that can be extracted from both the coupled model and observations. Given the prominence of this pattern in both the simulated and observed climates, a better understanding of the physical mechanisms associated with its existence is important, and this will be addressed in the following section.

4. Physical interpretation of the COWL pattern

a. Impact of air–sea interaction

WZR concluded that the contrast in thermal inertia between land and ocean is responsible for the existence of the COWL pattern. They reasoned that surface air temperatures over land are not as strongly damped by heat exchange with the underlying surface as are temperatures over sea. This land–sea difference in thermal capacity leads to much larger temperature fluctuations over land, such that the overall spatial mean temperature is disproportionately influenced by the anomalies occurring over land locations. This argument does not invoke any complex interactions between the atmosphere and ocean.

We first evaluate the potential role of air–sea interaction in generating the COWL pattern by comparing the results presented in the previous section, which are based on the output from a comprehensive atmosphere–ocean GCM (i.e., the coupled model), with their counterparts obtained from model runs with diminishing degrees of air–sea coupling. The latter runs have been examined in the study on climate variability by Manabe and Stouffer (1996). They include a 1000-yr integration of an atmospheric GCM coupled to a static oceanic mixed layer with a constant depth of 50 m, and a 500-yr integration of an atmospheric GCM with prescribed SST climatology at the air–sea interface. We shall henceforth refer to these experiments as the ML (mixed layer) and FS (fixed SST) runs, respectively.

In all of the integrations mentioned above the contrast in thermal inertia between land and ocean is represented. The atmospheric component of the model is also identical. The only important difference among the integrations is the degree of air–sea coupling. In the ML experiment, the air–sea interaction is restricted by allowing mixed layer temperatures to vary only as a result of heat exchanges with the model atmosphere directly aloft, and by allowing the atmosphere to respond to mixed layer temperature fluctuations. The mixed layer in a given grid box does not interact with those in neighboring boxes, nor is it coupled to any model of the deep ocean. The mixed layer is considered to be a motionless slab, so that momentum transfers associated with changes in the surface wind stress have no effect on it. Air–sea coupling is limited still further in the FS run, in which the climatological seasonal evolution of the observed SST field is assigned to all maritime grid points. The model atmosphere is hence subjected to the same annual cycle of SST conditions throughout the experiment.

The analysis procedure described in section 2 has been applied to the surface air temperature fields produced in the ML and FS runs. The data at all (land and ocean) grid points situated north of 20°N have been used in this analysis. The distributions of the spatial function $A(x)$ are shown in Fig. 6 for the (a) ML and (b) FS experiments. These patterns are almost identical to each other, and to that obtained from the output of the coupled model run (see Fig. 4). There are small variations in the fraction of temporal variance of $\overline{T}(t)$ explained by $\overline{A}T_1(t)$, as evident in Table 1. The smallest explained variance (39%) occurs in the ML integration, whose 50-m-deep mixed layer provides the smallest oceanic thermal inertia of the three integrations. The COWL-associated variance increases to 43% in the coupled model, in which the mixed layer is capable of thermal communication with the deep ocean. The variance fraction increases still further to 47% in the FS integration, where the prescribed SSTs represent an infinite source of thermal inertia. In view of the equally prominent COWL patterns in model environments with substantially reduced air–sea interaction, we are led to conclude that the land–sea contrast in thermal inertia is the most

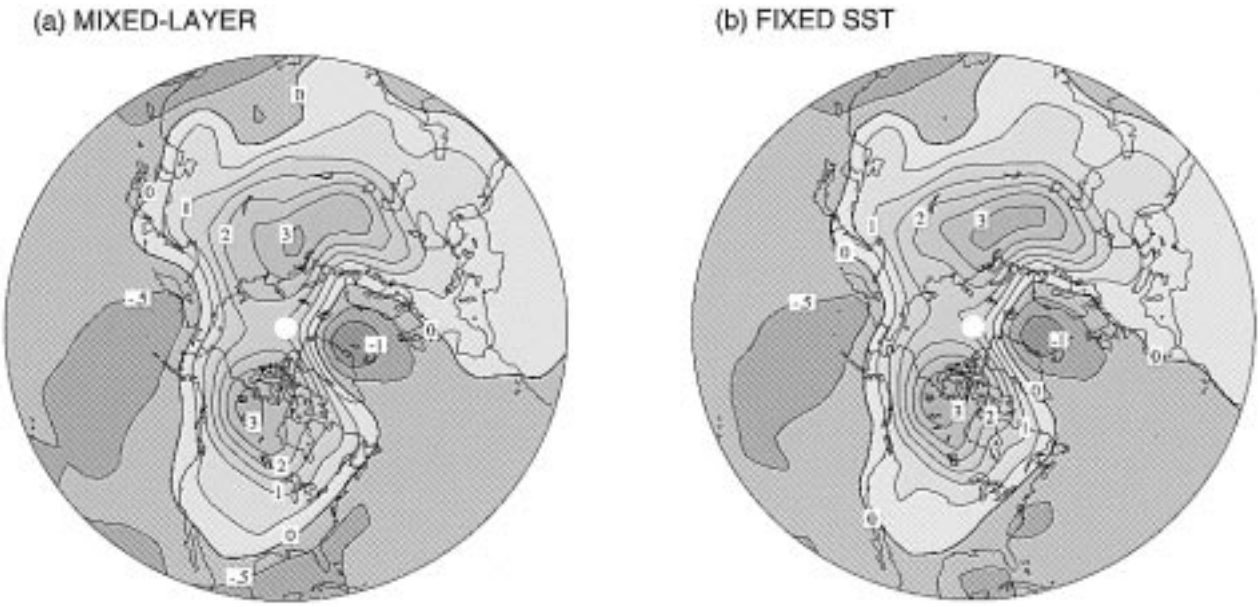

FIG. 6. Same as Fig. 4 except that surface air temperature is taken from experiments with an (a) atmosphere–mixed layer ocean model and (b) atmospheric model with prescribed SSTs.

important mechanism for the existence of the COWL pattern, and that the coupling between atmospheric and oceanic circulations does not play a critical role in producing such patterns.

b. Seasonal dependence of the COWL pattern

To document the seasonal variation in the amplitude and spatial structure of the COWL pattern, the data field $T(x, t)$ as well as the time series $T_1(t)$ for the coupled model experiment have been partitioned into two groups: the cold season (November–April) and the warm season (May–October). The domain of analysis used in deriving the time series $T_1(t)$ consists of all grid points located north of 20°N, and is the same as that used in constructing $A(x)$ in Fig. 4. The distributions of the regression coefficients of $T(x, t)$ on $T_1(t)$ for the (a) cold and (b) warm seasons are shown in Fig. 7. In this

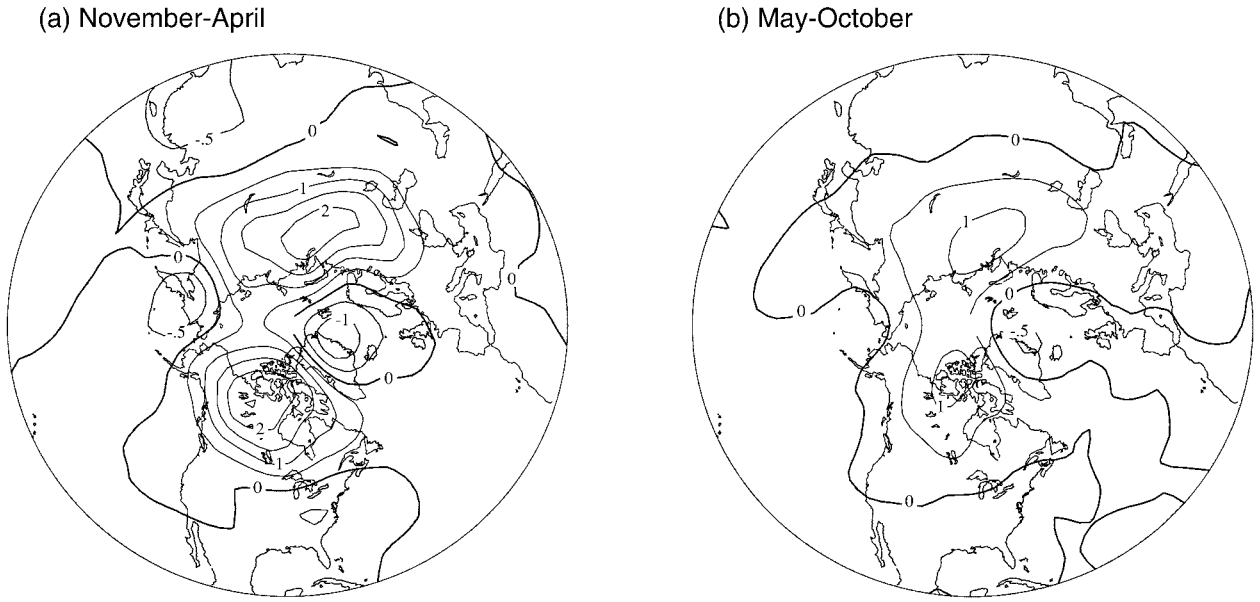

FIG. 7. Regression coefficients of $T(x, t)$ on $T_1(t)$ for (a) November–April, and (b) May–October, computed using data from the coupled model integration. Contour interval is 0.5°C. Areas with negative values are shaded.

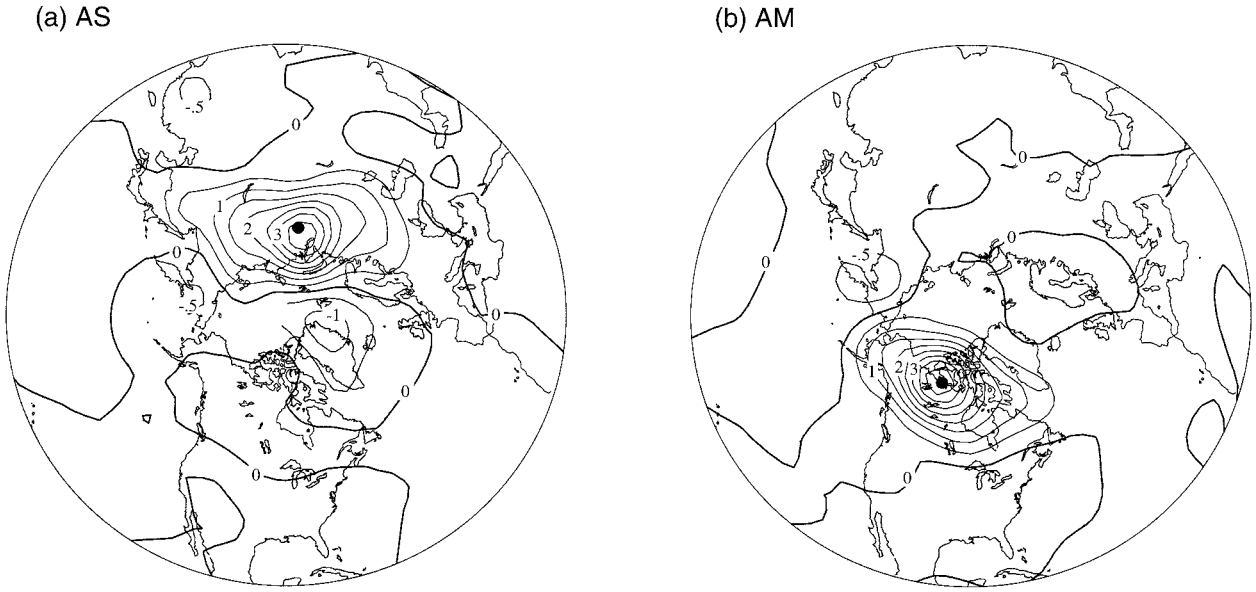

FIG. 8. Regression coefficients of $T(x, t)$ on $T(x_0, t)$ for x_0 located in (a) north-central Eurasia (64.4°N, 82.5°E; point AS), and (b) north-central North America (68.8°N, 112.5°W; point AM), as computed using the data from the coupled model integration. Contours and shading as in Fig. 7. Solid dots in (a) and (b) represent the locations of points AS and AM, respectively.

and other similar charts to be presented in this section, the regression coefficient of variable $a(x, t)$ on variable $b(t)$ is defined as $\langle a(x, t)b(t)\rangle/\sqrt{\langle b^2(t)\rangle}$, and may be interpreted as a measure of the typical amplitude of the change in a at point x associated with an anomaly of one standard deviation in b. (Here a and b represent departures from long-term averages.) Defining the regression coefficient in this way, which differs slightly from the standard definition, facilitates the comparison of regression analyses based on different independent variables.

Comparison between the two panels in Fig. 7 indicates that the spatial patterns of the local temperature variations accompanying $T_1(t)$ during the cold and warm seasons are very similar to each other. However, the typical magnitudes of the $T(x, t)$ anomalies in the cold season are greater than those in the warm season by approximately a factor of 2. Hence the fluctuations in both the areal average and the local deviations of surface temperature associated with $T_1(t)$ [i.e., $\overline{A}T_1(t)$ in Fig. 2a, and $T(x, t)$ in Fig. 7, respectively] attain largest amplitudes during the cold months. We shall therefore focus on the cold half of the year in the following discussion on the regional characteristics of the COWL pattern and the corresponding atmospheric circulation anomalies.

c. Regional components of the COWL pattern

The COWL pattern in the coupled model experiment during the cold season (Fig. 7a) is evidently hemispheric in scale, with multiple centers of action scattered throughout the domain of analysis. The degree of temporal covariability among the temperature fluctuations at these distant centers may be illustrated by mapping the regression coefficients (see definition in section 4b) of $T(x, t)$ at all x on $T(x_0, t)$ at a selected reference point x_0. The regression chart thus obtained depicts the pattern and amplitude of temperature perturbations at individual grid points associated with a temperature change of one standard deviation at x_0. Two reference sites have been chosen for the present analysis: the grid point in northern Asia, at 64.4°N, 82.5°E (hereafter referred to as AS), and the grid point in North America, at 68.8°N, 112.5°W (hereafter referred to as AM). These points correspond to the locations of the maxima appearing in Fig. 7a. The patterns of regression coefficients, as computed using monthly means of $T(x, t)$ from the coupled model run for the cold season only, are shown in Fig. 8 for x_0 located at (a) AS and (b) AM.

The distribution in Fig. 8a indicates that temperature fluctuations accompanying changes at AS attain noticeable amplitudes mostly in the Eastern Hemisphere, with anomalies in northern Eurasia being negatively correlated with those near Greenland, eastern China, and west of the Bering Strait. Particularly noteworthy is the near-zero correlation between the variations at AS and those in northern Canada. Conversely, it is evident from Fig. 8b that the anomaly pattern associated with the reference site at AM is confined mostly to the Western Hemisphere, where positive temperature changes over the northern portion of the North American landmass coincide with negative fluctuations over the eastern United States and west of the Bering Strait.

At first glance, the planetary-scale features associated with the COWL pattern (e.g., see Fig. 7a) seem to suggest the preferred occurrence of simultaneous temper-

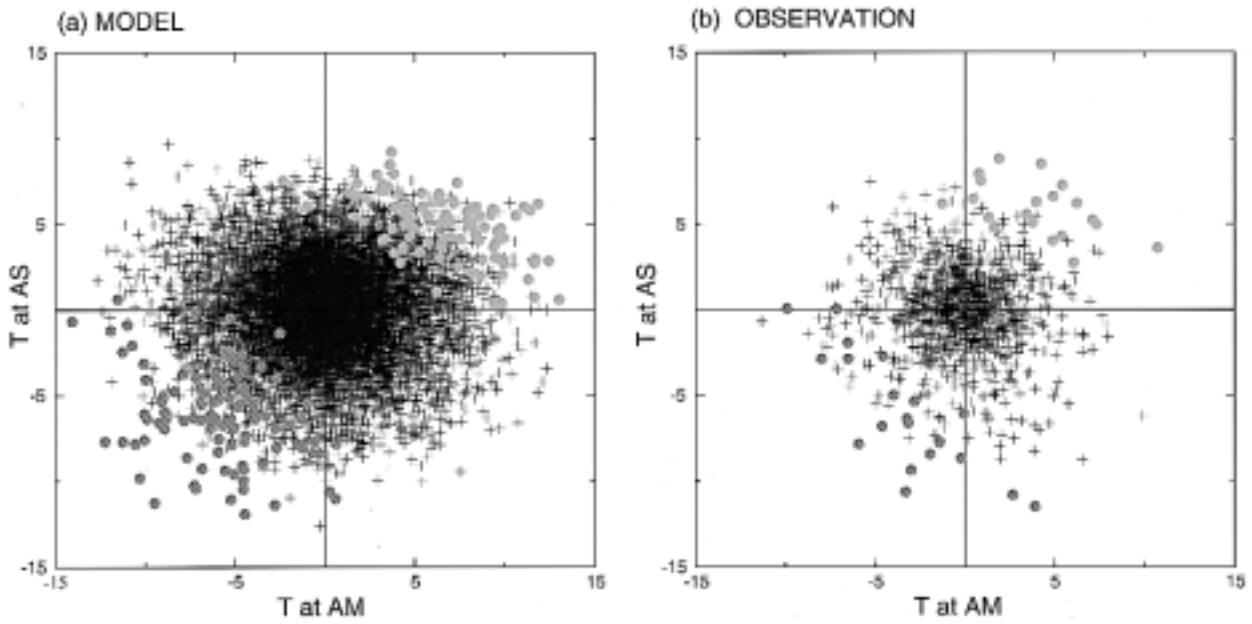

FIG. 9. Scatterplot of $T(x, t)$ at point AS vs $T(x, t)$ at point AM for (a) the 1000-yr coupled model simulation and (b) observations during the 1900–95 period. Each of the black crosses represents a single month. For the coupled model, red (blue) dots represent the 100 months with the highest (lowest) values of $T_1(t)$. For observations, red (blue) dots represent the 20 months with the highest (lowest) values of $T_1(t)$. Units are °C.

ature fluctuations spanning the entire Northern Hemisphere. Further diagnosis of the data by using a more regional approach, as presented in Fig. 8, reveals that the hemispheric temperature pattern related to COWL actually receives separate contributions from two distinct components. One of these components is organized about the temperature variations over Eurasia, and the other is prominent over North America only. The negligible temporal correlation between these two components implies that they occur almost independently of each other.

The relationships between the occurrence of the COWL pattern and temperature fluctuations at AS and AM may be further illustrated by the scatterplots constructed from the coupled model output (Fig. 9a). The abscissa and ordinate of this plot correspond to the $T(x, t)$ values averaged over the nine grid points surrounding AS and AM, respectively. The temperature fluctuations at this pair of sites during each month are represented in this plot by a black cross, so that the scatter diagram consists of altogether 12 000 data points. Those 100 months within this sample with the largest positive (negative) values of the temporal coefficients for the COWL pattern [i.e., $T_1(t)$] are highlighted by red (blue) dots. The time series for $T_1(t)$ has been obtained by analyzing the temperature data for all grid points situated north of 20°N. A similar plot is constructed based on observations (Fig. 9b), but in this case there are only 1152 monthly values plotted, with the 20 largest positive and negative values denoted by the colored dots.

Both scatterplots exhibit very similar characteristics. In each plot, the relative frequency of occurrence in each of the four quadrants of the coordinate system is approximately equal. This result is consistent with the weak linear correlation between temperature variations at AS and AM (see Fig. 8). The isotropic character of the distribution of the general population of points is in sharp contrast to the distribution of months with strong COWL signatures. Specifically, a large majority of the months with extreme positive values of $T_1(t)$ (red dots) reside in the upper-right quadrants of Figs. 9a and 9b, where positive anomalies at both AS and AM prevail. Similarly, most of the months with large negative values of $T_1(t)$ (blue dots) lie in the lower-left quadrants, where temperatures at both AS and AM are below normal. Very few months in the (just as densely populated) upper-left and lower-right quadrants, where the polarities of the temperature anomalies at AS and AM are opposite to each other, project strongly on the COWL pattern. It is hence evident that the COWL pattern preferentially occurs in a selective set of months with in-phase temperature variations over both the Eurasian and North American landmasses. Instances of out-of-phase temperature variations at these two continental sites are equally common. However, such cases would have a weak spatial projection on the COWL pattern, since the cancellations among the opposing temperature changes over Asia and North America would result in only small changes in $\overline{T}(t)$.

The recent study of Ting et al. (1996) has linked observed temperature fluctuations over the Asian and North American landmasses to the variability of the

Pacific and Atlantic jet streams, and to the zonally averaged zonal flow. Periods of out-of-phase temperature anomalies over the two continental sites (as depicted in the upper-left and lower-right quadrants of the scatterplots in Fig. 9) are characterized by in-phase fluctuations of the jet streams over the two ocean basins. Conversely, when temperature changes at AS and AM are of the same polarity (corresponding to the upper-right and lower-left quadrants in Fig. 9), the anomalies in the Pacific and Atlantic jet streams tend to oppose each other, thus resulting in a near-normal zonal-mean flow. Ting et al. (1996) further noted that fluctuations of the Pacific and Atlantic jets are temporally uncorrelated with each other. This finding is in accord with the independent temperature variations over Asia and North America seen in our study.

d. Relationships between temperature fluctuations and atmospheric circulation anomalies

The three-dimensional structure of the atmospheric circulation changes accompanying the surface temperature variations described in the previous subsections may be documented by mapping the regression coefficients (see definition in section 4b) of pressure or geopotential height data at selected levels on the relevant temperature indices. Figure 10 shows the patterns of such regression charts of sea level pressure (left column) and 500-mb height (right column) on $T_1(t)$ (Figs. 10a and 10d), $T(x_0, t)$ at reference site AS (Figs. 10b and 10e), and $T(x_0, t)$ at AM (Figs. 10c and 10f). All computations are based on monthly averages generated in the coupled model integration during the cold season. The time series $T_1(t)$ is obtained from the analysis of surface temperature data for all grid points located north of 20°N.

In accord with the negligible correlation between the temperature changes at AS and those at AM (see Fig. 8), there is almost no spatial overlap between the pressure and height anomalies accompanying the temperature changes at AS (Figs. 10b and 10e) and those corresponding to fluctuations at AM (Figs. 10c and 10f). The regression maps constructed using $T_1(t)$ (Figs. 10a and 10d) appear as a combination of the individual anomaly patterns associated with each of the two reference sites AS and AM.

The warm temperature anomalies at either the AS or AM sites individually (as in Fig. 8), or at both sites simultaneously (as in Fig. 7a), are coincident with below-normal sea level pressures at and to the west of the reference site(s) x_0 in question (see left panels of Fig. 10). The anomalous near-surface flow at and to the south of x_0 is directed either eastward or northeastward, and originates from relatively warmer maritime regions situated west of x_0. On the other hand, the cold anomalies near the Greenland and Bering Seas in Figs. 7 and 8 are under the influence of anomalous northerly airstreams to the west of the principal low pressure centers.

Inspection of the right panels in Fig. 10 reveals that the temperature changes at x_0 are also correlated with well-defined signatures in the middle troposphere. Warm anomalies at x_0 are accompanied at the 500-mb level by a positive height center to the east or southeast of x_0, and a negative center to the west of x_0. Comparison between the left and right columns of Fig. 10 indicates that the pressure–height perturbations have a distinctly baroclinic structure directly over both AS and AM, with considerable spatial displacements of the anomaly centers at 500 mb from those at sea level. Particularly noteworthy is the presence above AM of a positive anomaly in 500-mb height (Fig. 10f) and in 1000–500-mb thickness (not shown), thus indicating that the below-normal sea level pressure in that region (Fig. 10c) is characterized by a warm-core structure in the lower and middle troposphere. The baroclinic nature of geopotential height fluctuations with weekly and monthly timescales over the Eurasian and North American landmasses has previously been noted by Blackmon et al. (1979, see their Figs. 2, 3, and 12) and Hsu and Wallace (1985, their Figs. 2 and 5) for the observed atmosphere, and by Lau and Nath (1987, their Fig. 6) for the output from an atmospheric GCM similar to that examined here.

The amplitude of the simulated sea level pressure anomaly at AS and AM is comparable to that of the 500-mb height anomaly directly aloft (note that a pressure change of 1 mb is equivalent to a geopotential height change of approximately 8 m). This model finding is in agreement with the observation that the ratio of the standard deviation of 500-mb height to the standard deviation of 1000 mb height is close to unity in the vicinity of these reference sites (see Blackmon et al. 1979, their Fig. 4).

The near-zero or negative correlations between sea level pressure and 500-mb height anomalies in the vicinity of AS and AM are indicative of the occurrence of large fluctuations in the thickness field over these sites. This inference supports the identification by WZR (see their Fig. 4) and Wallace et al. (1996, see their Figs. 5 and 7) of high-amplitude thickness (or, equivalently, column-averaged temperature) fluctuations over the continents as a prominent signature of the COWL pattern.

e. Comparison of the simulated circulation patterns related to COWL with other observational and model results

The model patterns in Figs. 10a and 10d are in good agreement with the analogous regression charts based on observational data, as presented in Figs. 5 and 7 of Wallace et al. (1996). The pattern of Fig. 10e has the same spatial structure as a leading mode of variability of the atmospheric model used in the present coupled model experiment [see Fig. 2d of Ting and Lau (1993)]. This chart also exhibits some similarities to the observed northern Asian pattern (see Fig. 6a of Esbensen 1984),

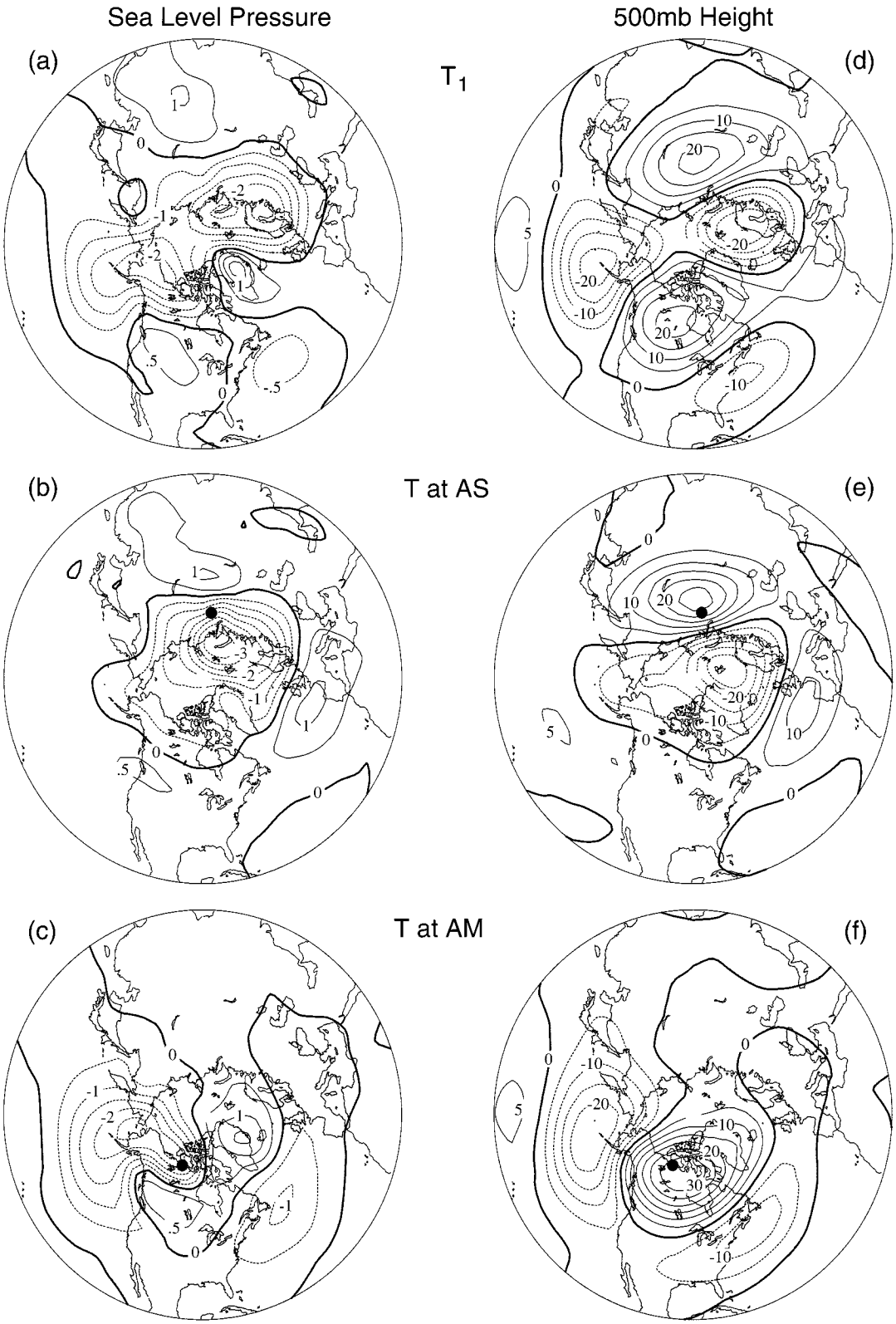

FIG. 10. Regression maps of sea level pressure on (a) $T_1(t)$, (b) $T(x, t)$ at AS, (c) $T(x, t)$ at AM, and 500-mb height on (d) $T_1(t)$, (e) $T(x, t)$ at AS, (f) $T(x, t)$ at AM, based on the coupled model integration. Contour intervals for the regression coefficients are 0.5 mb for sea level pressure and 5 m for 500-mb heights. Areas with negative values are shaded. Solid dots in (b) and (e) represent the location of point AS, and solid dots in (c) and (f) represent the location of point AM.

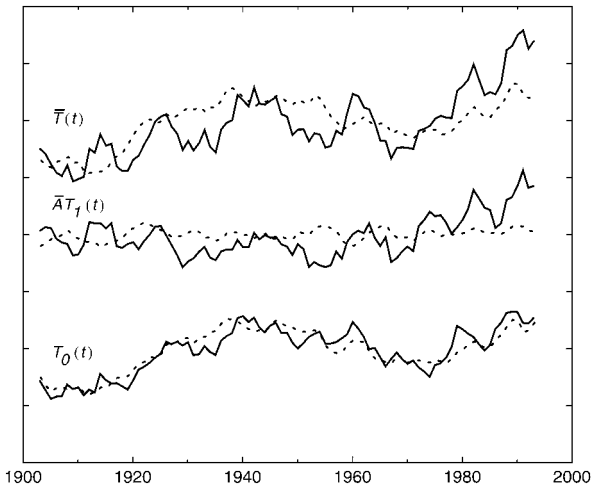

FIG. 11. Time series as in Fig. 2 but smoothed using a 5-yr moving average applied separately to cold (solid curve) and warm (dashed curve) season data. The interval between tick marks on the ordinate is 0.5°C.

and the Eurasian (type 1) pattern [see Fig. 7 of Barnston and Livezey (1987)]. The pattern of Fig. 10f is also known to be a recurrent pattern in the model atmosphere [see Fig. 2a of Ting and Lau (1993)]. This model result resembles an observed teleconnection pattern in the eastern North Pacific [see Fig. 11b of Esbensen (1984)], as well as the tropical–Northern Hemisphere pattern [see Fig. 5 of Barnston and Livezey (1987)]. The distribution in Fig. 10c is similar to that of the pressure changes accompanying the observed North Pacific oscillation (NAO) [see Fig. 12 of Rogers (1981)].

5. Nature of the recent positive trend in observed temperature

To examine the low-frequency behavior of $\overline{T}(t)$, $\overline{A}T_1(t)$, and $T_0(t)$ based on observations, 5-yr running averages of these quantities are computed (for the cold and warm seasons separately) from their monthly values, with the analysis domain confined to land poleward of 20°N (Fig. 11). (This corresponds to Fig. 5 of WZR, except that the temperature dataset has been extended through 1995 rather than ending in 1990.) The use of the running average filter effectively removes the high-frequency variations evident in Fig. 2.

WZR have pointed out the salient characteristics of these smoothed time series, including the larger variability of $\overline{T}(t)$ during the cold season, the similarity of cold and warm season $T_0(t)$ throughout the record, and the upward trend in cold season $\overline{A}T_1(t)$ that begins in the late 1960s. The extension of the analysis period through 1995 reveals that the latter trend has continued and reached 25 yr in length, with the smoothed $\overline{A}T_1(t)$ values in the early 1990s exceeding the previous peak reached in the early 1980s.

The continuation of the upward trend beyond the period analyzed by WZR is an intriguing aspect of the recent climate record. Is it larger than those trends that would be expected to result from the variability internal to the atmosphere–ocean system (i.e., that which would occur even in the absence of variations in radiative forcing)? To answer this question requires a good estimate of the internal climate variability. One factor that complicates such a determination using observational data is the relative brevity of the instrumental temperature record; a second is the likelihood that this record bears the imprint of both natural and anthropogenic changes in radiative forcing.

An alternative way to estimate the internal climate variability is to analyze the output from long climate model integrations conducted with no time variation in radiative forcing. Although the utility of this approach is predicated on the ability of the model to serve as a surrogate for the real climate system, it circumvents the difficulty of distinguishing between forced and internal variability inherent in the observed record, as well as the sampling problems associated with the brevity of the instrumental record. This methodology has been applied by Stouffer et al. (1994) and Manabe and Stouffer (1996) to assess the likelihood that the ongoing global temperature increase is due to internal climate variability. Santer et al. (1996) have applied an analogous approach to estimate the statistical significance of the similarity between observed climate changes and fingerprints of anthropogenic climate change generated by models.

Because the use of model output to estimate internal climate variability hinges upon the fidelity of the model, it is appropriate to closely examine the performance of the coupled model used in this study. We hereby review a number of studies that serve to demonstrate the ability of the coupled model to simulate climate fluctuations, both in terms of preferred modes of variability such as ENSO and the NAO, and fundamental quantities such as the standard deviation of surface air temperature.

Knutson et al. (1997) examined the simulation of the ENSO phenomenon in the coupled model and found that its life cycle is qualitatively consistent with the ''delayed oscillator'' mechanism that operates in realistic ENSO simulations conducted with high-resolution ocean models. However, the amplitude of ENSO variability in the coupled model is only about half of that observed. Variations in ENSO amplitude on multidecadal timescales also occur in the model, and these bear some similarity to observed variations based on instrumental, historical, and proxy records (Knutson and Manabe 1994; Knutson et al. 1997).

Lau and Nath (1994) examined the atmospheric response to tropical SST variability by forcing the atmospheric component of the coupled model with observed variations in tropical SST. They found a coupled mode of covariability between tropical SST and wintertime Northern Hemisphere midtropospheric circulation that closely resembles a corresponding mode de-

termined from observations. The amplitude of the atmospheric component of the simulated mode is smaller than its observed counterpart by a factor of 2 or 3, perhaps due to the underestimation in the model of stationary wave amplitude, degree of eddy-mean flow interactions in the extratropics, and precipitation anomalies in the Tropics. One can speculate that the difference between the simulated and observed variance fraction associated with the COWL pattern (see Table 1) may be related to some of these model deficiencies.

The coupled model also exhibits variability associated with the NAO. Both the spatial pattern and magnitude of sea level pressure fluctuations associated with the simulated NAO are very similar to observations, with a negative center in the vicinity of Iceland and a positive center extending from the Iberian Peninsula westward across the central North Atlantic (Delworth 1997, personal communication).

Surface air temperature variability in the coupled model has been examined by Manabe and Stouffer (1996). They found that the standard deviations of observed annual and 5-yr mean surface air temperature are approximately simulated for most of the area with available observations, with the exception of the tropical Pacific, where the underestimation of ENSO amplitude leads to a concomitant reduction in the variability of surface air temperature. The power spectrum of the simulated global mean surface air temperature was also found to be similar to the observed spectrum, except for an underestimation of power in the frequency band associated with ENSO variability.

Thus despite some deficiencies, the ability of the model in simulating the variability evident in the real climate system encourages us to utilize the unforced variability of the model to assess the magnitude of the recent trend in cold season $\overline{A}T_1(t)$ in the observations. Although a comparison of this trend with a model-derived estimate of unforced variability has implications for the detection of climate change, we do not intend to attribute the recent warming of Northern Hemisphere land to specific causes.

Observed trends in $\overline{A}T_1(t)$ are computed for overlapping windows of 15, 25, and 50 yr in length by performing linear least squares fits to the monthly values of $\overline{A}T_1(t)$ using only the values from cold season months (Fig. 12). The same procedure is applied to the 1000-yr integration of the coupled model (Fig. 13). Since there is no variation in radiative forcing during this integration, the resulting trends in $\overline{A}T_1(t)$ are unforced, and thus can be used to estimate the likelihood that internal variability of the coupled model would produce a trend of a given magnitude. If the coupled model and the real climate system have similar internal variability, as suggested by comparisons of simulated and observed variability (e.g., Manabe and Stouffer 1996), the results presented in Figs. 12 and 13 will allow us to evaluate the possibility that the observed trend in $\overline{A}T_1(t)$ has arisen by chance.

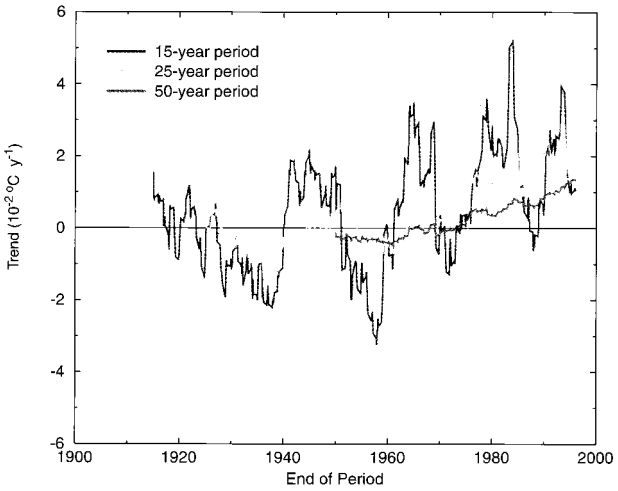

FIG. 12. Trends in $\overline{A}T_1(t)$ (10^{-2} °C yr^{-1}) for overlapping windows of various lengths based on surface air temperature observations for the period 1900–95 using land grid points north of 20°N. Trends are plotted with reference to the time at the end of the window. Green, red, and blue lines indicate window lengths of 15, 25, and 50 yr, respectively.

The rise in $\overline{A}T_1(t)$ since the late 1960s is reflected in the positive trends for all window lengths toward the end of the observed record (see Fig. 12). For the 25-yr window that most closely matches the duration of the recent upturn, the trend has a magnitude of over 2×10^{-2} °C yr^{-1} for much of the last decade. Even larger trends are evident over some 15-yr periods, although the variations in the trend on the 15-yr timescale are considerable. Very little systematic trend is noted during the first half of the record. For all three windows, the maximum positive trends occur over periods ending in the last 15 yr of the record.

In the coupled model integration, trends in $\overline{A}T_1(t)$ arise due to internal variability in the simulated climate system (see Fig. 13). The range of the trend amplitudes decreases with increasing period length, as would be expected in a system with little or no systematic trend. Trend values of 2.9×10^{-2}, 1.3×10^{-2}, and 0.5×10^{-2} °C yr^{-1} constitute the 99th percentile for period lengths of 15, 25, and 50 yr, respectively. Thus the observed 25-yr trend in cold season $\overline{A}T_1(t)$ during much of the last two decades exceeds the value corresponding to the 99th percentile. This finding does not necessarily imply that the observed trend is statistically significant at the 1% level for a variety of reasons, including the assumption that the simulated variability is comparable to that of the real climate system, and difficulties in estimating the number of degrees of freedom in a collection of trends based on overlapping windows.

For further comparison, the maximum and minimum values of the observed trend are plotted as the horizontal dashed lines in each panel of Fig. 13. For each window length, the maximum values substantially exceed the largest positive trends in the 1000-yr coupled model

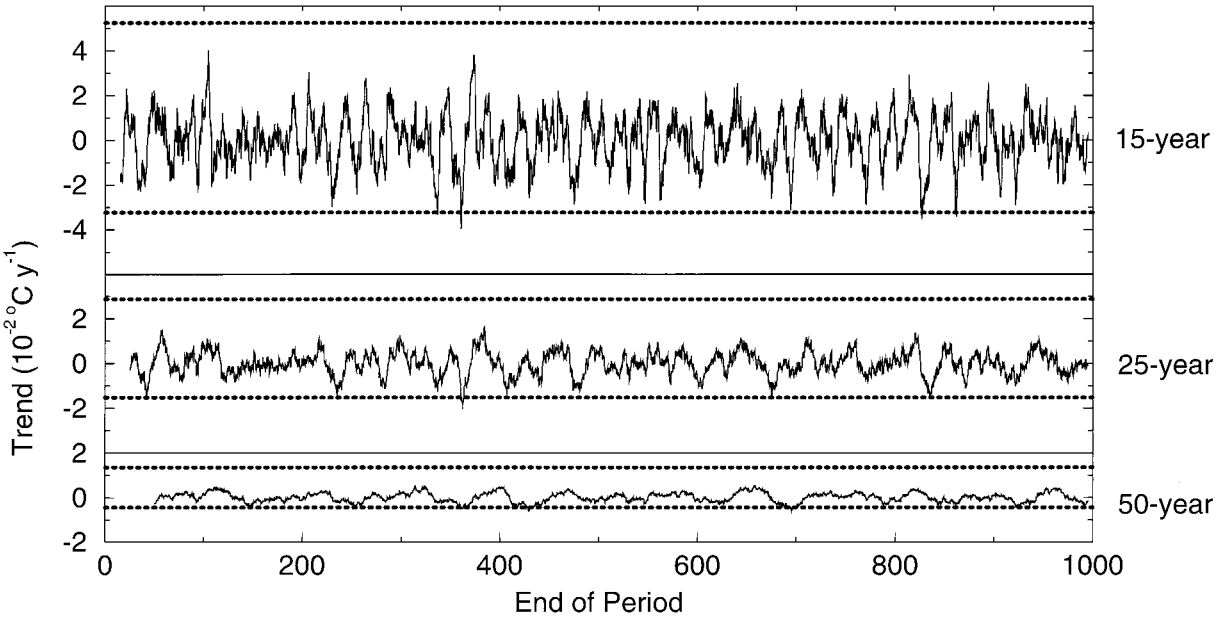

FIG. 13. Trends in $\overline{A}T_1(t)$ (10^{-2} °C yr^{-1}) for overlapping windows based on surface air temperature from the 1000-yr coupled model integration with constant forcing using land grid points north of 20°N for window lengths of 15 (top), 25 (center), and 50 (bottom) yr. Trends are plotted with reference to the time at the end of the window. The bold, dashed horizontal lines indicate the largest positive and negative trends in observed $\overline{A}T_1(t)$ for the period 1900–95.

integration. Although the standard deviation of $\overline{A}T_1(t)$ in the model is only 71% of the corresponding observed quantity, the substantial disparity in the magnitude of the observed trend and the largest trends in the 1000-yr integration seems to be greater than that which could be attributed to the underestimation of internal variability by the model. Thus our analysis supports the possibility that the recent upward trend in $\overline{A}T_1(t)$ may not be the result of unforced variability internal to the climate system.

6. Application of the analysis procedure of WZR to an integration with anthropogenic forcing

The results of the previous section suggest that the observed positive trend in $\overline{A}T_1(t)$ over the past 25 yr may not be associated with internal processes. If so, this would contradict the hypothesis of WZR that the component of temperature variability associated with the COWL pattern is a manifestation of atmospheric dynamics. To explore the possibility that this trend could be radiatively induced, we will apply the method of section 2 to a model integration in which a change in radiative forcing is imposed by design and thus the radiatively induced component of the simulated temperature change can be reliably estimated.

Haywood et al. (1997) have performed an integration of the same coupled model (see description in section 3) by prescribing temporal variations of the atmospheric greenhouse gas content and surface albedo. The greenhouse gas changes are based on past observations and estimates of future emissions, and the surface albedo changes are calibrated to mimic the effects of estimated past and future changes in tropospheric sulfate aerosols. This integration, subsequently denoted CO_2 + AER, is intended to crudely simulate the anthropogenic forcing of climate over the period 1766–2065. Haywood et al. (1997) provide a more detailed discussion of their experimental design.

The only difference in forcing between CO_2 + AER and the 1000-yr coupled model integration is the time-varying radiative forcing caused by CO_2 and aerosol changes. Thus we assume that any substantial long-term temperature trend that appears in CO_2 + AER is radiatively induced, given that the 1000-yr control integration does not contain such trends. By the same reasoning, any substantial long-term trend in $\overline{A}T_1(t)$ determined from the output of CO_2 + AER is assumed to be radiatively induced.

Surface air temperatures from land points located north of 20°N are extracted from that segment of CO_2 + AER that corresponds to the years 1900–2065. This model dataset is analyzed by the procedure defined in section 2, and 5-yr cold and warm season running averages of $\overline{T}(t)$, $\overline{A}T_1(t)$, and $T_0(t)$ are computed (Fig. 14). The hemispheric mean temperature $\overline{T}(t)$ undergoes an increase of ~0.8°C over the course of the twentieth century. This is comparable with the magnitude of the observed trend. Because of the dominating effect of future increases in greenhouse gases, an accelerated upward trend is evident in the next century, and $\overline{T}(t)$ rises

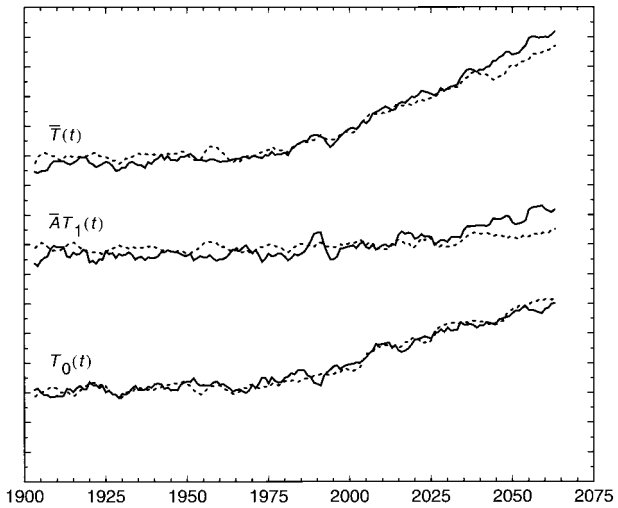

FIG. 14. Same as Fig. 11 except based on surface air temperatures from the CO_2 + AER integration for the period 1900–2065.

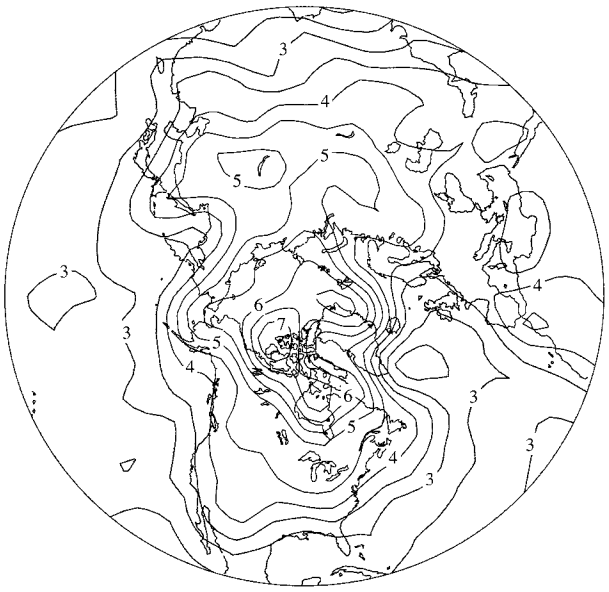

FIG. 15. Difference in annual mean surface air temperature between years 2045–65 of CO_2 + AER and the 1000-yr mean of the integration with constant forcing. Contour interval is 0.5°C. Areas with values less than 4°C are shaded.

to ~4°C above its 1900 level by the end of the integration.

When separated into the $\overline{A}T_1(t)$ and $T_0(t)$ components, most of the upward trend in $\overline{T}(t)$ in CO_2 + AER appears in the residual component $T_0(t)$, which experiences a rise of ~3°C over the course of the integration. The remainder of the trend is found in $\overline{A}T_1(t)$, which begins a steady increase toward the end of the twentieth century after a long period of little or no systematic trend. The rise in the $\overline{A}T_1(t)$ component from CO_2 + AER is larger in the cold season, a characteristic shared by the behavior of the observed $\overline{A}T_1(t)$ during the past 25 yr (see Fig. 11). By the early part of the next century, the magnitude of the trend in $\overline{A}T_1(t)$ from CO_2 + AER far exceeds the largest trends present in the 1000-yr coupled model integration with constant forcing (see Fig. 13).

The results from CO_2 + AER indicate that the radiatively induced warming is not confined to the $T_0(t)$ component of the time series of spatial mean temperature. One possible explanation for this finding is that the COWL pattern bears some similarity to the pattern of anthropogenic climate change, as noted by WZR. Thus the anthropogenic signal contained in CO_2 + AER could project positively on the COWL pattern and lead to an upward trend in $\overline{A}T_1(t)$. [In this context, the term COWL pattern is used only in reference to the $A(x)$ patterns computed from observations and the control integration.] To explore this possibility, we compare the $A(x)$ pattern extracted from the control integration (Fig. 1a) with the pattern of surface air temperature response to anthropogenic forcing, as estimated by the annual mean temperature difference (ΔT) between the period 2045–2065 from CO_2 + AER and the control integration (Fig. 15). There is broad similarity between these two patterns, with relatively large values over the northern continents and relatively small values over the oceans and at low latitudes. However, there are also subtle differences, such as the relatively large ΔT values over Greenland, the adjacent Nordic seas, and along the Siberian coast toward the Bering Sea, which are not found in the $A(x)$ pattern from the control integration. The pattern correlation between $A(x)$ and ΔT is 0.47 (Table 2) when computed over land points north of 20°N. As a consequence of this positive correlation, the increasing expression of the anthropogenic response during the course of the CO_2 + AER integration could lead to a positive trend in $\overline{A}T_1(t)$.

The effect of the spatial projection of the anthropogenic signal on the COWL pattern can be assessed by computing a ''hybrid'' time series in which $A^*(x)$ from the control integration is projected on $T^*(x, t)$ from CO_2 + AER. The product of this time series with $\overline{A}$ from the control integration, shown in Fig. 16 (solid curve), does exhibit a weak positive trend that begins at approximately the year 2000. The magnitude of the increase in this ''hybrid'' time series is less than 0.2°C,

TABLE 2. Matrix of spatial correlation coefficients among $A(x)$ from the 1000-yr coupled model integration (A_{control}), $A(x)$ for various segments of CO_2 + AER ($A_{1900–95}$, $A_{1900–2015}$, $A_{1900–2065}$), and the surface air temperature difference between years 2045 and 2065 of CO_2 + AER and the 1000-yr coupled model integration ($\Delta_{CO_2\ +\ AER}$). All patterns for $A(x)$ and $\Delta T_{CO_2\ +\ AER}$ are based on model data for land points north of 20°N. The computations are based on all months of the year.

	$A_{1900–95}$	$A_{1900–2015}$	$A_{1900–2065}$	$\Delta T_{CO_2\ +\ AER}$
A_{control}	0.98	0.94	0.74	0.47
$A_{1900–95}$		0.97	0.75	0.48
$A_{1900–2015}$			0.80	0.54
$A_{1900–2065}$				0.92

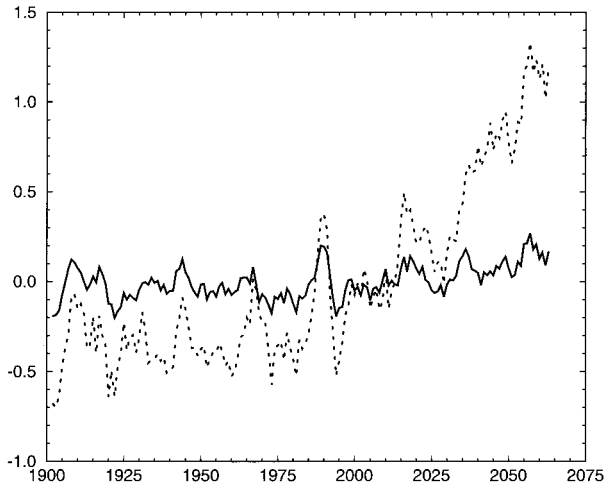

FIG. 16. ''Hybrid'' time series for the period 1900–2065 computed using the structure function $A(x)$ determined from the control integration and $T(x, t)$ values taken from CO_2 + AER (solid line). The actual $\overline{A}T_1(t)$ time series computed using both $A(x)$ and $T(x, t)$ from CO_2 + AER (dashed line) is shown for comparison. The computations are based on $T(x, t)$ from the cold season and a 5-yr moving average has been applied.

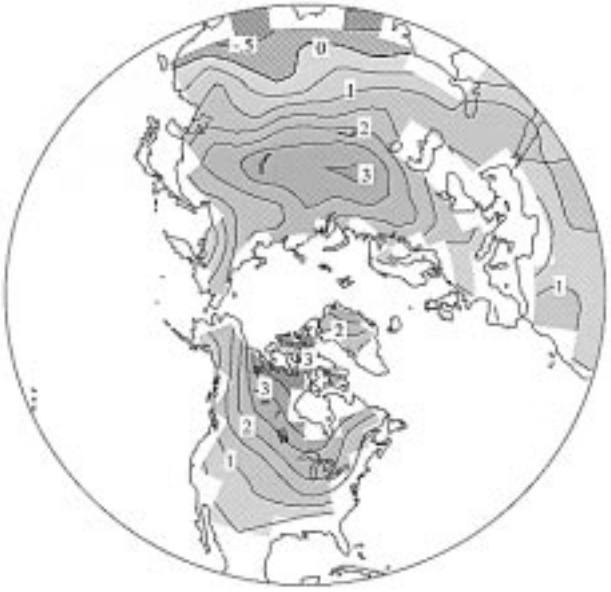

FIG. 17. Same as Fig. 1a except based on surface air temperatures from the CO_2 + AER integration for the period 1900–2065.

which is smaller by a factor of 5 than the increase in $\overline{A}T_1(t)$ of about 1°C during the same period when the latter quantity is computed entirely from CO_2 + AER (Fig. 16, dashed curve). Thus the spatial similarity between the anthropogenic response pattern and the COWL pattern accounts only for a small portion of the upward trend in $\overline{A}T_1(t)$ in CO_2 + AER.

Another possible explanation for the upward trend in $\overline{A}T_1(t)$ in CO_2 + AER is that there is a more fundamental problem in applying the methodology described in section 2 to climate data in which two separate processes, each with a characteristic spatial pattern, contribute substantially to the overall variability. CO_2 + AER contains two such processes: the internal atmospheric variability on relatively short timescales that produces the ''natural'' COWL pattern, and the anthropogenic radiative forcing. Since the current methodology can extract only a single pattern, the $A(x)$ pattern that results from its application to CO_2 + AER is likely a combination of the natural COWL pattern and the anthropogenic fingerprint. As such, the anthropogenic response will project strongly on the $A(x)$ pattern extracted from CO_2 + AER, leading to an upward trend in $\overline{A}T_1(t)$.

The above assertion can be substantiated by comparing the $A(x)$ pattern from the period 1900–2065 of CO_2 + AER (Fig. 17) with its counterpart from the control integration (Fig. 1a) and the pattern of anthropogenic response in surface air temperature ΔT (Fig. 15). The $A(x)$ pattern from CO_2 + AER is broadly similar to the control, but there are some important differences in the Arctic. Positive values along virtually all high-latitude coastal regions replace the negative $A(x)$ values of the control integration over northeastern Siberia, northern Alaska, Greenland, and eastern Canada. These differences increase the resemblance between $A(x)$ computed from CO_2 + AER and ΔT.

The interplay between the effects of anthropogenic radiative forcing and internal atmospheric variability is made evident by computing $A(x)$ patterns for different segments of CO_2 + AER each beginning in 1900. As the length of the segment increases, the pattern correlation between the $A(x)$ computed from that segment and $A(x)$ from the control integration decreases, reaching 0.74 for the segment covering the years 1900–2065 (Table 2). Conversely, the pattern correlation between the $A(x)$ patterns from the different segments of CO_2 + AER and the anthropogenic response pattern ΔT increases with increasing segment length, reaching 0.92 for the period 1900–2065 (Table 2). These results are consistent with an increasing imprint on $A(x)$ from the anthropogenic response pattern as CO_2 + AER proceeds. Thus the longer samples from this integration are more likely to yield an $A(x)$ pattern that is a mixture of the natural COWL pattern and the response to anthropogenic forcing.

These results clearly demonstrate that the analysis strategy used by WZR is incapable of separating the dynamically and radiatively forced variations in spatial mean surface air temperature in the presence of a strong radiative signal that possesses a distinct spatial pattern. This limitation exists because the analysis strategy is constrained to find a single pattern in the surface air temperature data that is most closely associated with variations in spatial mean temperature, and thus yields ambiguous results if two contributing patterns are present. It may not be necessary for the two patterns to be highly correlated with each other to cause this ambiguity, provided that the patterns are expressed in the

data with comparable magnitude. Only in the event that the response to radiative forcing is spatially uniform will this method yield a distinct separation of dynamically and radiatively induced variability.

7. Summary and discussion

By applying the same methodology that was developed by WZR to examine variations in observed temperatures, we have demonstrated that the COWL pattern can be simulated with a high degree of fidelity by a coupled atmosphere–ocean model with constant forcing. As in observations, fluctuations in the amplitude and polarity of this pattern account for a substantial fraction of the variability in hemispheric and global mean temperature on monthly timescales. By examining parallel integrations of models with more simplified oceanic components, we conclude that the contrast in thermal inertia between continents and oceans is the primary physical mechanism responsible for the COWL pattern.

The results presented in this paper have considerable relevance to the detection of climate change. The methodology we use constitutes a partitioning of the time series of spatial mean temperature into two components. One of these is associated with the variability of a characteristic spatial pattern; the other is the residual that remains after this fitting procedure. In their study of observed temperature variations, WZR suggested that radiatively induced temperature variations would be largely confined to the latter component. However, when we apply the methodology to a coupled model integration that incorporates the effects of changes in CO_2 and tropospheric sulfate aerosols (CO_2 + AER), a warming trend appears in both components. Thus we conclude that the decomposition associated with this methodology is not an appropriate way to isolate radiatively forced variations in temperature, and that some modification of the methodology would be required to make it more suitable for climate change detection.

The finding that the recent 25-yr positive trend in observed $\overline{A}T_1(t)$ is larger than any trends of comparable length from the control integration of the coupled model suggests that it may be due to some external forcing. This assessment is based on the use of the unforced variations from the coupled model as an estimate of unforced variability, and thus hinges upon the assumption that a model is an adequate surrogate for a real climate system. Because of our inability to clearly separate forced and unforced variability in the observed climate record, it is still difficult to fully evaluate this assumption. Perhaps the continued comparison of model simulations with climate observations will facilitate a more rigorous testing of this assumption, particularly if more accurate estimates of past variations in external forcing (i.e., tropospheric aerosol forcing, solar irradiance, volcanic effects, etc.) become available.

Other recent studies also suggest that recent changes in global temperature patterns may be associated with anthropogenic changes in atmospheric composition. Trenberth and Hoar (1996) reached such a conclusion based on their findings that both the recent trend for more ENSO events since 1976 and the prolonged tropical Pacific warming of the early 1990s are highly unlikely events in a statistical sense. The analysis of coupled climate simulations by Knutson and Manabe (1998) also suggests that anthropogenic forcing may have partially contributed to recent interdecadal trends in Pacific SST. Confirmation of these results using higher resolution model simulations and careful comparison with observations are necessary for ascertaining the physical origin for such long-term trends.

Several other issues that emerge from this work are worthy of further discussion. A very basic issue is the physical interpretation of the quantities that result from the methodology of WZR. In particular, there is some potential for confusion about the nature of the structure function $A(x)$. Unlike the spatial distributions that might emerge from the application of pattern recognition techniques (such as various forms of EOF analysis) to the same surface air temperature data, $A(x)$ does not describe a mode of variability of the climate system. Thus there is not necessarily any intercorrelation between the temperature anomalies in locations where $A(x)$ has the same sign, such as the positive centers over Eurasia and North America. The distinction between $A(x)$ and a preferred mode of variability was noted by Wallace et al. (1996), and is clearly illustrated by the teleconnection maps of Fig. 8 and the ensuing discussion.

A final issue regards the applicability of the decomposition method described in section 2 to other climate problems. Irrespective of whether or not this method is useful for separating dynamically induced variability from radiatively forced trends, we have demonstrated through analysis of the unforced 1000-yr coupled model integration that this technique can extract spatial structures that contribute significantly to areal-averaged temperature changes. Therefore this approach may be useful for identifying other internally generated patterns in long model integrations with constant forcing. One possibility would be to use averaging periods substantially longer than one month when determining the temperature anomalies. Since different physical mechanisms are expected to become prominent as the averaging period is increased, the $A(x)$ patterns based on longer averages should also be different. The regression maps of local surface air temperature on global mean surface air temperature [a spatial pattern linearly related to $A(x)$] calculated by Manabe and Stouffer (1996) using averaging periods of different lengths suggest a gradual shift from a pattern closely resembling the COWL pattern for 1-yr averages (their Fig. 19a) to a pattern emphasizing fluctuations over the high-latitude oceans for 25-yr averages (their Fig. 19b). They propose that surface air temperature fluctuations on longer timescales may be related to low-frequency oscillations in the North Atlantic thermohaline circulation. This illustrates that

the methodology used in this paper has potential utility in identifying mechanisms by which internally driven variations in spatial mean temperature are produced. The use of this methodology for such studies may prove to be valuable as additional long simulations of unforced climate variability are undertaken in the future.

Acknowledgments. The authors thank J. M. Wallace for generously providing encouragement, technical advice, and comments on an earlier version of this paper. S. Manabe, R. Stouffer, and J. Haywood provided the output from their model integrations. Y. Zhang and D. Thompson provided valuable technical advice concerning the analysis method and its application to observations. Comments and suggestions from T. Delworth, M. Hoerling, T. Knutson, J. Lanzante, J. Mahlman, M. Mann, R. Stouffer, and an anonymous reviewer were valuable in improving the manuscript.

APPENDIX

Computational Details

Here we describe the procedure for computing the spatial pattern $A(x)$ and the time series $T_1(t)$ as introduced in section 2. The function $A^*(x)$ can be determined by multiplying both sides of Eq. (3) by $\overline{T}(t)$ and then performing a temporal average, and by making use of Eq. (2) and the orthogonality constraint in Eq. (4). We obtain

$$\langle \overline{T}(t)T^*(x, t)\rangle \equiv C^*(x) = \langle T_1^2(t)\rangle \overline{A}\, A^*(x) + \langle \delta^*(x, t)\overline{T}(t)\rangle. \quad \text{(A1)}$$

By making the additional assumption that $\langle \delta^*(x, t)\overline{T}(t)\rangle = 0$, so that the temporal covariance between $\overline{T}(t)$ and $T^*(x, t)$ [i.e., $C^*(x)$ on the lhs of Eq. (A1)] receives no contribution from the space–time variability of the residual $\delta^*(x, t)$, Eq. (A1) then reduces to

$$C^*(x) = \langle T_1^2(t)\rangle \overline{A} A^*(x). \quad \text{(A2)}$$

By requiring that $\delta^*(x, t)$ be temporally uncorrelated with $\overline{T}(t)$, the spatial structure of the covariance function $C^*(x)$ is seen to be solely determined by $A^*(x)$. Upon normalization of the amplitude of $A^*(x)$ to unity [i.e., $\overline{A^{*2}(x)} = 1$], $A^*(x)$ may be obtained as

$$A^*(x) = \frac{C^*(x)}{[\overline{C^{*2}(x)}]^{1/2}}. \quad \text{(A3)}$$

To compute the common time series of expansion coefficients $T_1(t)$ for the spatial pattern $A(x)$ and its constituents [$\overline{A}$ and $A^*(x)$, see Eq. (1)–(3)], we next multiply Eq. (3) by $A^*(x)$ and perform a spatial average. Noting the orthogonality condition in Eq. (5), we then have

$$T_1(t) = \overline{A^*(x)T^*(x, t)}. \quad \text{(A4)}$$

Finally, the constant $\overline{A}$ can be evaluated by multiplying Eq. (2) by $T_1(t)$, performing a temporal average, and applying the constraint in Eq. (4), thus yielding

$$\overline{A} = \frac{\langle \overline{T}(t)T_1(t)\rangle}{\langle T_1^2(t)\rangle}. \quad \text{(A5)}$$

Noting that both $\overline{T}(t)$ and $T_1(t)$ have zero temporal means, the form of Eq. (A5) indicates that $\overline{A}$ is actually the slope of the linear regression of $\overline{T}(t)$ upon $T_1(t)$.

In summary, the spatial pattern $A(x)$ and its expansion coefficients $T_1(t)$ are obtained in the following sequence: the function $A^*(x)$ is first computed using Eqs. (A1) and (A3); the expansion coefficients $T_1(t)$ are then obtained from Eq. (A4); and the constant $\overline{A}$ is determined by Eq. (A5). Finally, the pattern $A(x)$ is constructed by adding $\overline{A}$ to $A^*(x)$. Note that the methodology as outlined above allows for the specification of only one such spatial pattern.

As noted in WZR, the above procedure is equivalent to a singular value decomposition (SVD) analysis [see Bretherton et al. (1992) for details]. The left and right input data fields are $\overline{T}(t)$ and $T^*(x, t)$, with spatial dimensions of 1 and N, respectively. Here N represents the number of grid points in the domain of interest. Application of a SVD on the $1 \times N$ temporal covariance matrix between $\overline{T}(t)$ and $T^*(x, t)$ [i.e., $C^*(x)$, see Eq. (A1)] yields $C^*(x) = \sigma \mathbf{l}\mathbf{r}^{\mathrm{T}}(x)$, where σ is the singular value, and $\mathbf{l}$ and $\mathbf{r}(x)$ are the left and right singular vectors, with dimensions of 1 and N, respectively. Comparison between this expression for $C^*(x)$ and Eq. (A2) reveals that $A^*(x)$ has the same spatial structure as $\mathbf{r}(x)$. The temporal expansion coefficients for the left field are obtained by projecting $\mathbf{l}$ (a constant) on $\overline{T}(t)$, and have the same temporal structure as $\overline{T}(t)$. The expansion coefficients for the right field are evaluated by spatially projecting $\mathbf{r}(x)$ [or $A^*(x)$] on $T^*(x, t)$, and have the same temporal structure as $T_1(t)$ [see Eq. (A4)]. By construction, $\mathbf{l}$ and $\mathbf{r}(x)$ explain the maximal mean-square temporal covariance between $\overline{T}(t)$ and $T^*(x, t)$. The dimensionality of the input data fields is such that only one pair of singular vectors can be obtained by this method.

REFERENCES

Barnston, A. G., and R. E. Livezey, 1987: Classification, seasonality and persistence of low-frequency atmospheric circulation patterns. *Mon. Wea. Rev.*, **115,** 1083–1126.

Blackmon, M. L., R. A. Madden, J. M. Wallace, and D. S. Gutzler, 1979: Geographical variations in the vertical structure of geopotential height fluctuations. *J. Atmos. Sci.*, **36,** 2450–2466.

Bretherton, C. S., C. Smith, and J. M. Wallace, 1992: An intercomparison of methods for finding coupled patterns in climate data. *J. Climate*, **5,** 541–560.

Delworth, T. L., S. Manabe, and R. J. Stouffer, 1993: Interdecadal variations of the thermohaline circulation in a coupled ocean–atmosphere model. *J. Climate*, **6,** 1993–2011.

Esbensen, S. K., 1984: A comparison of intermonthly and interannual teleconnection in the 700 mb geopotential height field during the Northern Hemisphere winter. *Mon. Wea. Rev.*, **112,** 2016–2032.

Haywood, J. M., R. J. Stouffer, R. T. Wetherald, S. Manabe, and V. Ramaswamy, 1997: Transient response of a coupled model to estimated changes in greenhouse gas and sulfate concentrations. *Geophys. Res. Lett.*, **24,** 1335–1338.

Hsu, H.-H., and J. M. Wallace, 1985: Vertical structure of wintertime teleconnection patterns. *J. Atmos. Sci.,* **42,** 1693–1710.

Jones, P. D., and K. R. Briffa, 1992: Global surface air temperature variations during the twentieth century. Part 1: Spatial, temporal and seasonal details. *Holocene,* **2,** 174–188.

Knutson, T. R., and S. Manabe, 1994: Impact of increased CO_2 on simulated ENSO-like phenomena. *Geophys. Res. Lett.,* **21,** 2295–2298.

——, and ——, 1995: Time-mean response over the tropical Pacific to increased CO_2 in a coupled ocean–atmosphere model. *J. Climate,* **8,** 2181–2199.

——, and ——, 1998: Model assessment of decadal variability and trend in the tropical Pacific Ocean. *J. Climate,* **11,** 2273–2296.

——, ——, and D. Gu, 1997: Simulated ENSO in a global coupled ocean–atmosphere model: Multidecadal amplitude modulation and CO_2 sensitivity. *J. Climate,* **10,** 138–161.

Lau, N.-C., 1981: A diagnostic study of recurrent meteorological anomalies appearing in a 15-year simulation with a GFDL general circulation model. *Mon. Wea. Rev.,* **109,** 2287–2311.

——, 1985: Modeling the seasonal dependence of the atmospheric response to observed El Niños in 1962–76. *Mon. Wea. Rev.,* **113,** 1970–1996.

——, and M. J. Nath, 1987: Frequency dependence of the structure and temporal development of wintertime tropospheric fluctuations—Comparison of a GCM simulation with observations. *Mon. Wea. Rev.,* **115,** 251–271.

——, and ——, 1994: A modeling study of the relative roles of tropical and extratropical SST anomalies in the variability of the global atmosphere-ocean system. *J. Climate,* **7,** 1184–1207.

Manabe, S., and D. G. Hahn, 1981: Simulation of atmospheric variability. *Mon. Wea. Rev.,* **109,** 2260–2286.

——, and R. J. Stouffer, 1993: Century-scale effects of increased atmospheric CO_2 on the ocean–atmosphere system. *Nature,* **364,** 215–218.

——, and ——, 1994: Multiple-century response of a coupled ocean–atmosphere model to an increase of atmospheric carbon dioxide. *J. Climate,* **7,** 5–23.

——, and ——, 1996: Low-frequency variability of surface air temperature in a 1000-year integration of a coupled atmosphere-ocean-land surface model. *J. Climate,* **9,** 376–393.

——, ——, M. J. Spelman, and K. Bryan, 1991: Transient responses of a coupled ocean–atmosphere model to gradual changes of atmospheric CO_2. Part I: Annual mean response. *J. Climate,* **4,** 785–818.

——, M. J. Spelman, and R. J. Stouffer, 1992: Transient responses of a coupled ocean-atmosphere model to gradual changes of atmospheric CO_2. Part II: Seasonal response. *J. Climate,* **5,** 105–126.

Mann, M. E., and J. Park, 1994: Global-scale modes of surface temperature variability on interannual to century timescales. *J. Geophys. Res.,* **99,** 25 819–25 833.

——, and ——, 1996: Joint spatiotemporal modes of surface temperature and sea level pressure variability in the Northern Hemisphere during the last century. *J. Climate,* **9,** 2137–2162.

——, ——, and R. S. Bradley, 1995: Global interdecadal and century-scale climate oscillations during the past five centuries. *Nature,* **378,** 266–270.

Parker, D. E., P. D. Jones, C. K. Folland, and A. Bevan, 1994: Interdecadal changes of surface temperature since the late nineteenth century. *J. Geophys. Res.,* **99,** 14 373–14 399.

Philander, S. G., 1990: *El Niño, La Niña, and the Southern Oscillation.* Academic Press, 293 pp.

Rasmusson, E. M., and T. H. Carpenter, 1982: Variations in tropical sea surface temperature and surface wind fields associated with the Southern Oscillation/El Niño. *Mon. Wea. Rev.,* **110,** 354–384.

Rogers, J. C., 1981: The North Pacific oscillation. *J. Climatol.,* **1,** 39–57.

Santer, B. D., and Coauthors, 1996: A search for human influences on the thermal structure of the atmosphere. *Nature,* **382,** 39–46.

Schlesinger, M. E., and N. Ramankutty, 1994: An oscillation in the global climate system of period 65–70 years. *Nature,* **367,** 723–724.

Stouffer, R. J., S. Manabe, and K. Bryan, 1989: Interhemispheric asymmetry in climate response to a gradual increase of atmospheric CO_2. *Nature,* **342,** 660–662.

——, ——, and K. Ya. Vinnikov, 1994: Model assessment of the role of natural variability in recent global warming. *Nature,* **367,** 634–636.

Ting, M., and N.-C. Lau, 1993: A diagnostic and modeling study of the monthly mean wintertime anomalies appearing in a 100-year GCM experiment. *J. Atmos. Sci.,* **50,** 2845–2867.

——, M. P. Hoerling, T. Xu, and A. Kumar, 1996: Northern Hemisphere teleconnection patterns during extreme phases of the zonal-mean circulation. *J. Climate,* **9,** 2614–2633.

Trenberth, K. E., and J. W. Hurrell, 1994: Decadal atmosphere–ocean variations in the Pacific. *Climate Dyn.,* **9,** 303–319.

——, and T. J. Hoar, 1996: The 1990–1995 El Niño–Southern Oscillation event: Longest on record. *Geophys. Res. Lett.,* **23,** 57–60.

Wallace, J. M., Y. Zhang, and J. A. Renwick, 1995: Dynamic contribution to hemispheric mean temperature trends. *Science,* **270,** 780–783.

——, —— and L. Bajuk, 1996: Interpretation of interdecadal trends in Northern Hemisphere surface air temperature. *J. Climate,* **9,** 249–259.

Zhang, Y., J. M. Wallace, and D. S. Battisti, 1997: ENSO-like interdecadal variability. *J. Climate,* **10,** 1004–1020.